Basin-Scale, High-Wavenumber Sea Surface Wind Fields from a Multiresolution Analysis of Scatterometer Data

TOSHIO M. CHIN, RALPH F. MILLIFF, AND WILLIAM G. LARGE

National Center for Atmospheric Research, Boulder, Colorado

(Manuscript received 19 August 1996, in final form 19 August 1997)

ABSTRACT

A numerical technique sensitive to both spectral and spatial aspects of sea surface wind measurements is introduced to transform the irregularly sampled satellite-based scatterometer data into regularly gridded wind fields. To capture the prevailing wavenumber characteristics (power-law dependence) of sea surface wind vector components, wavelet coefficients are computed from the scatterometer measurements along the satellite tracks. The statistics of the wavelet coefficients are then used to simulate high-resolution wind components over the off-track regions where scatterometer data are not available. Using this technique, daily wind fields with controlled spectral features have been produced by combining the low-wavenumber wind fields from ECMWF analyses with the high-wavenumber measurements from the *ERS-1* scatterometer. The resulting surface wind fields thus reflect nearly all available measurements affecting surface wind, including the synoptic surface pressure. The new surface wind forces a basin-scale quasigeostrophic ocean model such that the average circulation and energetics are consistent with the previous studies, in which purely synthetic high-wavenumber wind forcing was used.

1. Introduction

Numerical models of the ocean general circulation are typically driven by climatological wind datasets of coarse resolution in both space and time (e.g., Hellerman and Rosenstein 1983). Increasingly popular alternatives to climatology are the global, six-hourly, analyzed surface winds produced by numerical weather prediction centers, such as the European Centre for Medium-Range Weather Forecasting (ECMWF) and the National Centers for Environmental Prediction (NCEP). Recently, spaceborne scatterometers have made available sea surface wind measurements at a higher spatial resolution over larger areas than previously possible. By *synthesis* of high-wavenumber wind components, Milliff et al. (1996) have demonstrated that circulation patterns and energetics of a quasigeostrophic (QG) ocean model are sensitive to high-wavenumber spectral content expected in wind data from scatterometers. Such models also respond in important ways to wind forcing on timescales as short as a few days (Large et al. 1991).

The primary focus of this paper is to produce global/basin-scale surface wind fields with both the frequency and wavenumber content required by ocean general circulation models. The strategy is to combine surface wind analyses from ECMWF with scatterometer winds from the European Space Agency's *ERS-1* satellite. The frequency of the former is more than adequate for our purposes. The remaining technical problem to be addressed here is that of interpolating/extrapolating the high-wavenumber variability that is sampled irregularly by the *ERS-1* satellite throughout the model domain.

The satellite scatterometer wind measurements,[1] with swath widths of at most 1500 km, need to be interpolated between swaths before forcing a typical ocean circulation model. For the purpose of examining the effects of high-wavenumber wind forcing on ocean dynamics, the interpolation method must preserve the spectral characteristics of the measurements. A simple, piecewise constant (in time) scheme, such as that used successfully by Barnier et al. (1994) to force some aspects of seasonal cycles in the Indian Ocean, can nevertheless retain the ''bandlike'' patterns of measurement discontinuities that affect spatial spectral characteristics of the wind-forcing field. A more conventional interpolation scheme based on space–time smoothing can also smear out storm-scale spatial structures in the wind curl patterns, compromising the spectral characteristics of the surface wind (Large et al. 1991; Mariano and Brown 1992).

Our wind products are the results of joint interpola-

Corresponding author address: Toshio M. Chin, RSMAS/MPO, University of Miami, 4600 Rickenbacker Causeway, Miami, FL 33149.
E-mail: tchin@rsmas.miami.edu

[1] The ADEOS/NSCAT satellite scatterometer (Naderi et al. 1991) was operational from mid-September 1996 to mid-June 1997.

tion of wind analyses and measurements, combined with selective use of statistical extrapolation. The term ''composition'' is used herein to indicate such complementary use of interpolation and extrapolation. The surface wind composition technique presented in this paper is based on spectral models (''power laws'') predicted by the two-dimensional (2D) turbulence theory (Leith 1971) and observed as prevailing characteristics of sea surface wind (Freilich and Chelton 1986). To numerically capture these spectral features of surface wind, the composition method employs a wavelet-based spectral analysis for fractal random processes (Wornell 1993). Wavelet analyses are particularly useful for study of turbulent flows because they are simultaneously space and wavenumber specific (Farge 1992). While this wavenumber specificity enables development of a composition method based on spectral characterization of the wind data, the spatial specificity makes wavelet analysis a flexible numerical tool to address the highly irregular and concentrated sampling patterns of the scatterometer measurements as well as natural intermittency in the wind.

The input datasets in our wind composition problem are described in section 2. Section 3 contains the mathematical background for our interpolation and spectral analysis techniques. A wavelet-based spectral analysis of the scatterometer wind measurements is then presented in section 4. Sections 5 and 6 describe, respectively, four datasets of composed sea surface wind fields and corresponding responses of an ocean circulation model to wind forcing. Section 7 then summarizes the main results.

2. Surface wind observations

The time variability and low-wavenumber content of all the composed fields are based on the ECMWF surface (10-m height) wind analyses. Diverse coincidental meteorological observations (ship, buoy, and aircraft data, as well as balloon soundings and satellite retrievals) have been assimilated to produce these analyzed fields. We utilize one year (1 July 1992–30 June 1993) of vector wind fields, sampled daily (at 1200 UTC) and preinterpolated from the nominally 1.125° Gaussian grid onto a regular 1° grid that extends 100° east–west and 42° north–south over the North Atlantic basin.

The *ERS-1* scatterometer has a swath width of about 500 km, with nominal spatial resolutions of 25 km across-track (a row of 19 independent wind samples) and 48 km alongtrack (Attema 1991). Figure 1 shows a typical *ERS-1* surface wind sampling pattern for a 24-h period over the North Atlantic. The spatial coverage is heterogeneous and, at most, 20% of the basin is sampled during any 24-h period. The figure also exemplifies occasional data loss due to various postprocessing issues (Freilich and Dunbar 1993a,b), most notably instrumental insensitivity to wind speed below about 2 m s^{-1} as well as ambiguity among two to four solutions for wind direction. Also, the long-term sampling pattern of

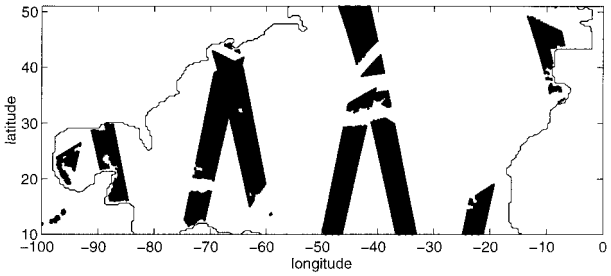

FIG. 1. A typical *ERS-1* scatterometer sampling pattern for a 24-h period over the North Atlantic model domain.

ERS-1 contains a persistent data void in the northeastern section of the domain, as shown in Fig. 2, due to systematic switch-off of the scatterometer.

Spatial variability of the surface wind can be studied statistically using 2D turbulence theory (Leith 1971) and expressed in terms of (isotropic) spectral energy densities $E(k)$ with respect to wavenumbers $k \geq 0$. Under the classic turbulence theories, the spectral energy density functions obey the so-called power law, $E(k) \propto k^{-\gamma}$, where the exponent γ is a constant over a range of k. Indeed, Freilich and Chelton (1986) observed, in the Seasat scatterometer measurements of surface wind over the tropical and midlatitude Pacific, that the zonal and meridional components of wind vectors each satisfy a power law with $\gamma \approx 2$ for a wavelength range of 200–2200 km ($k \approx 0.003 \sim 0.03$ rad km^{-1}). Recently, similar power laws (for the same wavelength range) in the *ERS-1* scatterometer wind data have been reported (Freilich and Pazdalski 1995). Our verifications of these power laws using both the traditional discrete Fourier transform and wavelet analysis are presented later. In contrast, the ECMWF wind fields display the ''$\gamma \approx 2$'' power law only down to wavelengths of about 900 km or up to wavenumbers of about 0.007 rad km^{-1}. The power-law failure at spatial scales significantly larger than the grid spacing in the ECMWF fields is presumably due to the numerical smoothing inherent in the analysis procedure and/or model dynamics.

In the following, ''high wavenumber'' refers to the Fourier–spectral band measurable with scatterometers but not available in most analysis fields produced by meteorological forecast models (with respect to the $\gamma \approx 2$ power law). For our particular case, therefore, the high-wavenumber range corresponds to wavelengths from the ECMWF drop-off at about 900 km down to the (along-track) Nyquist interval for the *ERS-1* scatterometer measurements, which is about 100 km, that is, a wavenumber range of approximately 0.007 to 0.06 rad km^{-1}. This spectral band also corresponds roughly to a wavelength range of 8°–1° and therefore contains the most energetic scales of the midlatitude ocean eddies.

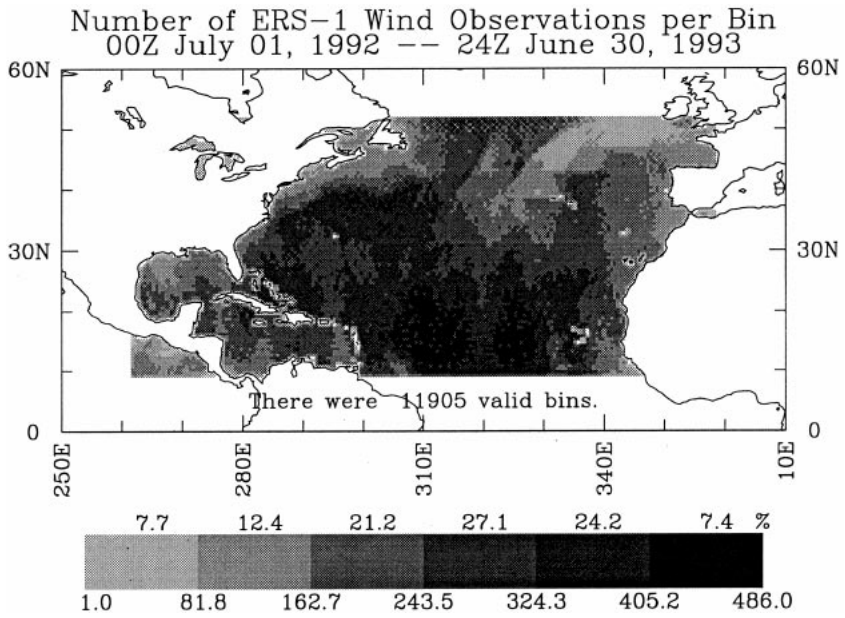

FIG. 2. Number of *ERS-1* scatterometer samples (valid data) in each of 1/2° × 1/2° bins for the 1-yr period over the North Atlantic domain. Note the ''edges'' in the sampling pattern in the northeastern to north-central regions due to some systematic void in observation.

3. Multiresolution analysis and fractal spectrum

Our ultimate goal is to compare ocean model responses to various wind-forcing inputs characterized by distinct wavenumber spectra. The focus of this paper is the means by which wavenumber-controlled wind fields are obtained. The wind-forcing fields are produced from the daily ECMWF analyses, the *ERS-1* scatterometer data, and the spectral statistics of the scatterometer data. The particular wind-forcing fields (four sets of yearlong, daily fields) are summarized in Table 2 and detailed in section 5. This section presents a technical background for our methodology.

The ECMWF and *ERS-1* wind datasets have quite different sampling patterns and resolutions. To combine the two, an interpolator must provide a common mathematical platform for the respective resolutions. Furthermore, the interpolator must allow access to the wavenumber content of the wind fields in a spatially selective manner, as the ''high-wavenumber'' data from the scatterometer are available only beneath satellite orbits (Fig. 1). These tasks of multiscale interpolation and spatially selective spectral analysis can be accomplished under a single mathematical framework of *multiresolution analysis* (Mallat 1989; Daubechies 1992; Heijmans 1993), which has originally been conceptualized by Meyer and Mallat as a unifying framework for the theories of orthonormal wavelet transforms. From the beginning, development of wavelet transforms has been intimately connected with modeling and processing of geophysical signals, and many authors including Daubechies (1992) and Farge (1992) have surveyed categories and variations of the wavelet transforms. The orthonormal wavelets, with their energy conservation property, are particularly suited for spectral analysis. Their applications in conjunction with turbulence theory have been investigated (Meneveau 1991; Yamada and Ohkitani 1991; Farge 1992). In particular, physical processes displaying power-law spectra can be considered as *fractal*, or statistically self-similar, random processes. Such processes exhibit strong long-distance correlation structures that can be captured with orthonormal wavelets much more readily than with more traditional, regression-type statistical models (Wornell 1993).

In our approach, multiresolution analysis is implemented with the *B-spline* polynomial functions (Prenter 1975; Wahba 1990), whose capability to generate orthonormal wavelet transforms (Unser and Aldroubi 1992) is especially useful for the wavenumber-sensitive interpolation/extrapolation problem at hand. Standard polynomial splines such as B splines are also generally applicable to interpolation of irregularly sampled data such as the scatterometer measurements. In the remainder of the paper, $u(x, y)$ and $v(x, y)$ denote the zonal and meridional wind vector components, respectively, where x and y are the zonal and meridional spatial indices. The wavenumber-controlled spline representations for the respective wind components are denoted as $\hat{u}(x, y)$ and $\hat{v}(x, y)$.

a. Multiresolution analysis

We begin with a brief general description of the multiresolution analysis. For conciseness, we consider a generic real-valued scalar function $u(x)$ over a 1D domain.

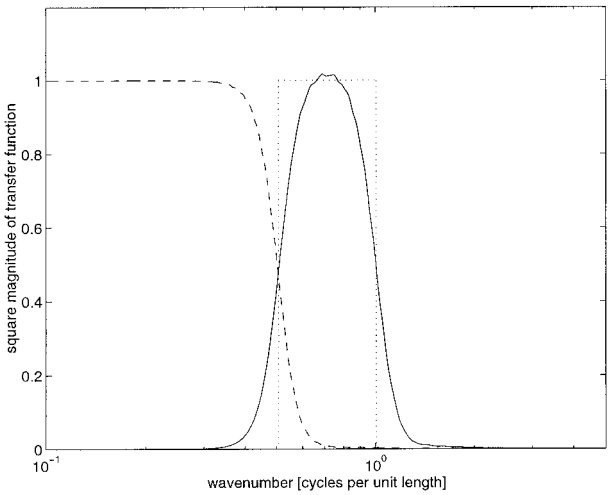

FIG. 3. The characteristic wavenumber-spectra for the spline approximation $\hat{u}_j(x)$ (dashed line) and scale difference $u'_j(x)$ (solid line) for the unit scale of $\Delta_j = 10^0$. The dotted line represents a least square fit of ideal bandpass filter to the scale-difference spectrum.

Extension to a 2D domain is straightforward and described later (section 3c).

The multiresolution analysis consists of a sequence of approximation (spline function) spaces

$$\cdots \subset V_{-2} \subset V_{-1} \subset V_0 \subset V_1 \subset V_2 \subset \cdots,$$

where V_j is the space of functions smoothly approximated at a given resolution parameterized by the integer j. In essence, V_j specifies and contains a low-pass filtered version, $\hat{u}_j(x) \in V_j$, of the signal $u(x)$, as depicted in Fig. 3. Incrementally finer details of the signal are represented in V_j as j increases. The approximation spaces are specified by self-similarity that leads to a fractal representation of the signal. Each approximation space contains a scaled version of the same function, and this scaling value is traditionally chosen to be the smallest nontrivial positive integer, 2. Thus, for an arbitrary function $f(x)$,

$$f(x) \in V_j \quad \text{if and only if} \quad f(2x) \in V_{j+1} \qquad (1)$$

for all integers j. Under this construct, the inherent length-scale Δ_j of the approximated functions in V_j is given by

$$\Delta_j = 2^{-j}\Delta_0, \qquad (2)$$

which also defines the ''resolution'' of the approximation space for a given reference length Δ_0. The scale parameter Δ_j has the same length unit as x and, as we will see, it also determines a ''characteristic wavelength'' associated with the resolution index j. For the surface wind composition problem, we use $\Delta_0 = 111.2$ km, which corresponds to 1° of latitude.

A wavenumber-dependent decomposition of a signal can be achieved in terms of the scale-difference signal

$$u'_j(x) \equiv \hat{u}_{j+1}(x) - \hat{u}_j(x). \qquad (3)$$

The space of such difference signals is in the wavelet space, denoted as W_j. Formally, the wavelet space W_j is the orthogonal complement of the approximation space V_j within the next larger space V_{j+1}:

$$V_j \perp W_j, \qquad V_j \cup W_j = V_{j+1},$$

where $\hat{u}_{j+1} \in V_{j+1}$, $\hat{u}_j \in V_j$, and $u'_j \in W_j$. Thus, all the incremental ''details'' of the signal beyond an arbitrary resolution of J are contained in the *mutually orthogonal* wavelet spaces W_J, W_{J+1}, W_{J+2}, . . . , so that the nonoverlapping union

$$V_J \cup W_J \cup W_{J+1} \cup W_{J+2} \cup \ldots$$

completely represents the space of all real-valued functions, or

$$u(x) = \hat{u}_J(x) + \sum_{j=J}^{\infty} u'_j(x). \qquad (4)$$

As exemplified in Fig. 3, $u'_j(x)$ is essentially a bandpass filtered version of the signal $u(x)$, and the multiresolution decomposition (4) can be considered as a quantized spectral analysis of $u(x)$ for the scales finer than J. The resolving power of this spectral analysis, or equivalently the effective bandwidth of the bandpass filters, is determined by the self-similar scaling factor of 2 to be $(2\Delta_j)^{-1}$ cycles per unit length for a given j. This implies a trade-off in using a wavelet spectrum as opposed to the traditional Fourier spectrum: The bandwidth doubles for each increment in j for a wavelet spectrum, while it remains constant for a discrete Fourier transform. A wavelet-based spectral analysis, however, gains spatial specificity (totally lacking in the Fourier-based methods) in exchange for this loss in wavenumber resolution, as governed by the uncertainty principle (Meneveau 1991). Spatial specificity is critical in addressing the irregular swath patterns of *ERS-1* scatterometer data.

1) IMPLICIT NOISE MODEL

Measurement noise is most frequently modeled as an additive zero-mean process that has finer-scale variabilities than the signal of interest. The portion of noise removed by a common low-pass filtering or smoothing operation (e.g., most optimal filters in practice) corresponds to the finescale components of the actual measurement error. This standard treatment of measurement noise does not seem applicable to the multiresolution decomposition (4) that models the signal, at least conceptually, to infinitely fine scales. In practice, however, there is always an upper limit on the resolution of interest, say $J_{\max}$, so that the finer-scale signal components $u'_j(x)$, $j > J_{\max}$, would not be parts of the signal representation and hence be implicitly designated as ''noise'' in this traditional sense.

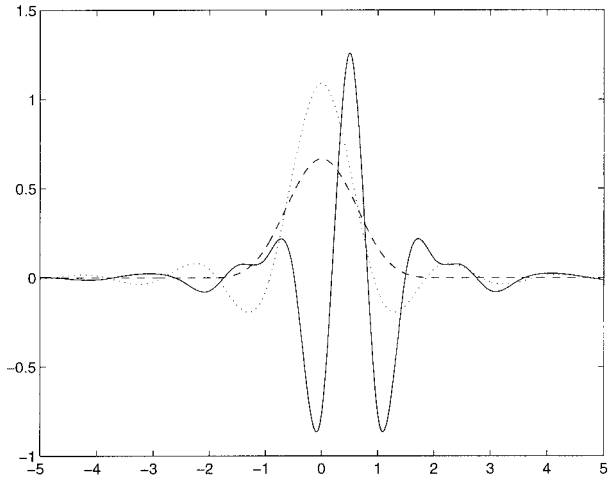

FIG. 4. The basis generating functions: $\beta(x)$ (dashed line), $\phi(x)$ (dotted line), and $\psi(x)$ (solid line).

2) BASIS FUNCTIONS

All basis functions in the multiresolution analysis used here are generated from the three functions depicted in Fig. 4—the B-spline function $\beta(x)$ and the Battle–Lemarié (BL) scaling $\phi(x)$ and wavelet $\psi(x)$ functions (Battle 1987; Lemarié 1988). Both the B-spline $\beta(x)$ and BL scaling $\phi(x)$ functions generate sets of basis functions that span the approximation space V_j, but the two functions have different features and hence utilities as elaborated below. The BL wavelet function $\psi(x)$ generates bases that span the wavelet space W_j. The three basis generating functions used here are piecewise *cubic* polynomials with continuous first and second derivatives, which have been applied to a variety of interpolation/analysis problems (Prenter 1975; Inoue 1986; Meneveau 1991). The cubic B-spline function is given as

$$\beta(x) = \begin{cases} \frac{1}{6}(x+2)^3, & -2 \le x \le -1, \\ \frac{2}{3} - x^2\left(1 + \frac{x}{2}\right), & -1 \le x \le 0, \\ \frac{2}{3} - x^2\left(1 - \frac{x}{2}\right), & 0 \le x \le 1, \\ -\frac{1}{6}(x-2)^3, & 1 \le x \le 2, \\ 0, & \text{otherwise}, \end{cases} \tag{5}$$

and the third-order BL (BL-3) functions $\phi(x)$ and $\psi(x)$ (of Fig. 4) can be derived from the cubic $\beta(x)$ as detailed in appendix A. Piecewise linear, quadratic, and higher-order polynomials for alternative $\beta(x)$, $\phi(x)$, and $\psi(x)$ are given elsewhere (Unser and Aldroubi 1992; Daubechies 1992).

In multiresolution analysis, the basis functions are obtained by scaling and translation of a generating function as

$$\beta_{jm}(x) \equiv 2^{j/2}\beta\left(\frac{x}{\Delta_j} - m\right) \tag{6}$$

$$\phi_{jm}(x) \equiv 2^{j/2}\phi\left(\frac{x}{\Delta_j} - m\right) \tag{7}$$

$$\psi_{jm}(x) \equiv 2^{j/2}\psi\left(\frac{x}{\Delta_j} - m\right), \tag{8}$$

where scaling and translation are parameterized by j and m, respectively. Note, for a given j, a unit translation is determined by the scale parameter Δ_j, for example, $\psi_{j,m+1}(x) = \psi_{jm}(x - \Delta_j)$. For each j, therefore, there is a grid with the spacing Δ_j, and a basis function is centered at each grid point. These basis functions establish a multiresolution representation of the signal $u(x)$ with their expansion coefficients. The spline approximation $\hat{u}_j(x)$ and scale difference $u'_j(x)$ for each j are represented by series expansions as

$$\hat{u}_j(x) = \sum_m b_{jm}\beta_{jm}(x) \in V_j, \tag{9}$$

$$= \sum_m c_{jm}\phi_{jm}(x) \in V_j, \tag{10}$$

and

$$u'_j(x) = \sum_m d_{jm}\psi_{jm}(x) \in W_j. \tag{11}$$

All basis functions are spatially localized (Fig. 4), leading to space specificity of the multiresolution analysis.

The B-spline representation (9) of the approximation space is essentially a standard interpolation technique. The B-spline function is a nonnegative, weighting (distribution) function [$\beta(x) \ge 0$, $\int_{-\infty}^{\infty} \beta(x)\,dx = 1$], which is generally suitable as an interpolator, and it also has a compact support {$\beta(x) = 0$ for $x \notin [-2, 2]$ for the cubic B spline}, which is desirable for numerical efficiency. On the other hand, the BL scaling-function expansion (10) of the same approximation space is useful for its energy conservation property since the wavelet and scaling basis functions are mutually *orthonormal* (normalized to the reference length Δ_0) as

$$\int_{-\infty}^{\infty} \psi_{jm}(x)\psi_{jm'}(x)\,dx = \int_{-\infty}^{\infty} \phi_{jm}(x)\phi_{jm'}(x)\,dx = \begin{cases} \Delta_0, & m = m', \\ 0, & m \ne m'. \end{cases} \tag{12}$$

All the basis functions are dimensionless, so that the respective expansion coefficients b_{jm}, c_{jm}, and d_{jm} not only carry the essential information of the original signal but also inherit its physical unit as well (e.g., meters per second for our surface wind composition problem). Given the multiresolution decomposition (4), either co-

efficient set $\{b_{Jm}\}_m$ or $\{c_{Jm}\}_m$, along with the wavelet coefficient sets $\{d_{jm}\}_m$ for $j \geq J$, would completely specify the original signal $u(x)$. As mentioned earlier, the BL coefficient sets $\{c_{Jm}\}_m$ and $\{d_{jm}\}_m$ conserve the square magnitude (''energy'') of the signal.

3) Computation of the coefficients and their statistics

A variety of methods exist to compute the B-spline coefficients $\{b_{jm}\}_m$ for a given j based on the samples $\{(x_k, u_k)\}_k$ of the function $u(x)$. Because of the highly irregular sampling pattern of the scatterometer data, we employ a standard variational approach (Inoue 1986) summarized in appendix B. By orthonormality, the coefficients of scaling/wavelet expansions can be derived by the inner products

$$c_{jm} = \frac{1}{\Delta_0}\int_{-\infty}^{\infty} u(x)\phi_{jm}(x)\,dx \tag{13}$$

and

$$d_{jm} = \frac{1}{\Delta_0}\int_{-\infty}^{\infty} u(x)\psi_{jm}(x)\,dx. \tag{14}$$

In practice, $u(x)$ in these inner products must be interpolated/approximated from the sampled data, for example, by the B spline.

To control spectral energy densities of the composed wind fields, we are interested in obtaining statistics of the wavelet coefficients d_{jm} from the scatterometer data, so that signal components $u_j'(x)$ at some prescribed scales Δ_j can be synthesized using (11) by randomly generated wavelet coefficients that obey the measured statistics. The second-order statistics of the wavelet coefficients can be obtained directly from the interpolated signals $\hat{u}_j(x)$ and, in particular, their scale differences. To this end, consider the wavelet expansion (11) of a sampled scale-difference signal $u_j'(x)$ over the domain $x \in [0, L]$. Because the basis functions are spaced by an interval of Δ_j, the number M of the wavelet coefficients is L/Δ_j. By orthonormality of $\{\psi_{jm}(x)\}_m$, we then have an equation analogous to Parseval's theorem for Fourier series

$$\frac{1}{L}\int_0^L (u_j')^2\,dx = \frac{\Delta_0}{L}\sum_{m=1}^{M}(d_{jm})^2 = 2^j\left(\frac{1}{M}\sum_{m=1}^{M}(d_{jm})^2\right), \tag{15}$$

which leads to a relationship between the mean-square values of the wavelet coefficients and corresponding scale-difference signal

$$\overline{(d_j)^2} = 2^{-j}\overline{(u_j')^2} \tag{16}$$

for each j, where the overbar denotes *spatial* averaging (over x or m). Since the averages of $u_j'(x)$ over x and d_{jm} over m are typically zero [as $\int_{-\infty}^{\infty}\psi(x)\,dx = 0$], (16) yields estimates of the variances of the wavelet coefficients given the scale-difference signal computed as (3). Scale-dependent estimates of the variance based on (16) are used to constrain our composition procedure (sections 4 and 5).

4) Dilation relationship

A key property of the B-spline functions that makes them especially suitable for the multiresolution analysis is the *dilation relation*, which equates the basis function at a given resolution with a finite linear combination of basis functions at the next finer resolution (Unser and Aldroubi 1992). Specifically, the dilation relation for the cubic B spline (depicted in Fig. 4) is

$$\beta(x) = \frac{1}{8}\beta(2x-2) + \frac{1}{2}\beta(2x-1) + \frac{3}{4}\beta(2x) + \frac{1}{2}\beta(2x+1) + \frac{1}{8}\beta(2x+2), \tag{17}$$

which allows direct projection of coarse-resolution spline coefficients to coefficients in a higher-resolution space,

$$b_{j+1,2m} = \frac{1}{8\sqrt{2}}(b_{j,m-1} + 6b_{j,m} + b_{j,m+1})$$

$$b_{j+1,2m+1} = \frac{1}{2\sqrt{2}}(b_{j,m} + b_{j,m+1}). \tag{18}$$

The implication is that even though the inherent sampling interval in the dataset dictates the upper limit of the resolution at which the spline coefficients can be computed directly, the spline representation at an arbitrarily high resolution can be obtained (without resampling the coarse-level splines) using (18). In particular, the coarse ECMWF data are splined this way to combine with the finer-resolution scatterometer data (section 5).

b. Spectral analysis of fractal random processes

Wavenumber sensitivity and self-similarity make the wavelet-based multiresolution analysis especially suitable for study of fractal random processes governed by a spectral energy density function of the form

$$E(k) = E_0 k^{-\gamma}, \qquad k \geq 0,\ \gamma > 0, \tag{19}$$

where E_0 is a constant. If $u(x)$ is such a process, then there will be a similar geometric ''law'' in the scale-dependent energies (square magnitudes) of the bandpass signal components $u_j'(x)$. Indeed, the fractal-spectral properties detailed by Wornell (1993) indicate that the intrascale variance of the wavelet coefficients $\{d_{jm}\}_m$ satisfies a discrete power law,

$$\text{var}_m(d_{jm}) \propto 2^{-j\gamma} = \left(\frac{\Delta_0}{\Delta_j}\right)^{-\gamma}, \tag{20}$$

where $\text{var}_m(\cdot)$ denotes the variance taken over the spatial index m. Conversely, a signal synthesized from a set of wavelet coefficients with the geometrically scale-dependent variances (20) would closely approximate a fractal process with the same power-law exponent γ in (19). Because an orthogonal wavelet analysis quantizes the wavenumber space, the Fourier spectrum of a wavelet-synthesized signal exhibits some systematic ripples over the ideal fractal spectrum (19). Wornell's results indicate that the magnitude-bound of such ripples tends to grow as γ increases.

The exact relationship between wavelet-based and Fourier-based spectral energy densities is difficult to establish and is dependent on two application-specific scenarios—the wavenumber resolution of the particular wavelet function in use and the form of the spectral density function $E(k)$. The BL-3 wavelets (appendix A, Fig. 4), based on cubic polynomials, are known to have a reasonable wavenumber resolution (Unser and Aldroubi 1992) and have been applied to studies of turbulence (Meneveau 1991). Using higher-order polynomials (among other approaches) can enhance wavenumber resolution by increasing the *regularity*[2] of the wavelet. Wavelet bases with high regularity might be desirable for extreme cases of modeling fractal processes with large γ (Wornell 1993) and over very fine scales (Perrier et al. 1995).

To examine the effect of the shape of $E(k)$ on wavelet-based spectral density, assume that $u_j'(x)$ is an ideally bandpassed version of the signal over $k \in [\alpha k_j, \lambda k_j]$, where the characteristic wavenumber k_j is given as $k_j \equiv 1/\Delta_j$. For the BL-3 wavelet, a least square fit (Fig. 3) yields $\alpha = 0.52$ and $\lambda = 1.00$. The ideal bandpass approximation then leads to

$$\overline{(u_j')^2} \approx \int_{\alpha k_j}^{\lambda k_j} E(k)\, dk = \varepsilon_\gamma k_j E(k_j), \tag{21}$$

using the particular form of $E(k)$ satisfying the power law (19), where

$$\varepsilon_\gamma = \begin{cases} (\lambda^{1-\gamma} - \alpha^{1-\gamma})/(1-\gamma), & \gamma \neq 1, \\ \log(\lambda/\alpha), & \gamma = 1, \end{cases} \tag{22}$$

where log is the natural logarithm. Then, from (16), we have the relation between the Fourier energy density and wavelet coefficient energy

$$\begin{aligned} E(k_j) &= \varepsilon_\gamma^{-1}\overline{(u_j')^2}\,\Delta_j, \\ &= \varepsilon_\gamma^{-1}\overline{(d_j)^2}\,\Delta_0. \end{aligned} \tag{23}$$

[2] Wavelet functions with higher regularity have faster rates of decay away from the wavenumbers of support in the Fourier domain (Wornell 1993).

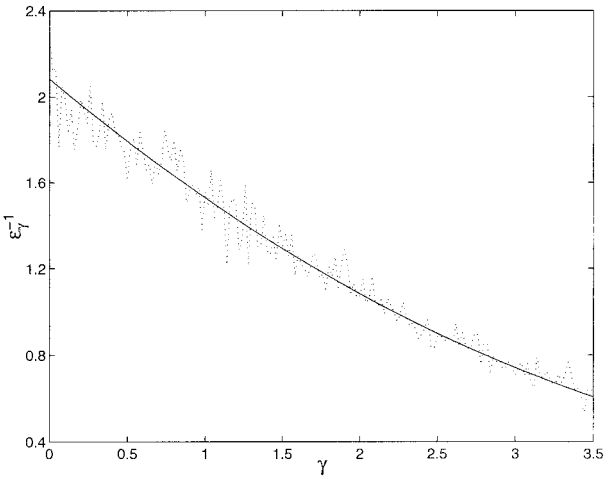

FIG. 5. A plot of ε_γ^{-1} as given by (22). The dotted line represents numerically simulated ratios of $E(k_j)$ to $\overline{(u_j')^2}\Delta_j$ for the shown range of γ.

The dimensionless multiplicative factor ε_γ^{-1} is plotted for a range of γ in Fig. 5, showing that numerical simulation (wavelet energies computed for Fourier-synthesized fractal processes) agrees generally well with (22). Thus, to estimate samples of a (fractal) spectral energy density function from wavelet coefficients, a value of γ must be preestimated from (20) to obtain ε_γ^{-1}.

The multiresolution method of spectral energy estimation (23) certainly lacks the wavenumber resolution of standard methods based on discrete Fourier transforms; however, due to spatial locality of the wavelet bases it tends to be robust against the edge effects (Fourier methods usually require "windowing" to pretaper the ends of the signal). Also, while irregularly sampled (often the case over multidimensional spaces) datasets usually require preinterpolation for spectral estimation, the effects of smoothing in interpolation are quite explicit in the multiresolution approach, which in fact incorporates interpolation procedures.

c. Two-dimensional multiresolution analysis

The basis functions for the 2D approximation space V_j are just the tensor products of the 1D version described previously, leading to the expansions

$$\hat{u}_j(x, y) = \sum_m \sum_n B_{jmn}\beta_{jm}(x)\beta_{jn}(y) \in V_j, \tag{24}$$

$$= \sum_m \sum_n C_{jmn}\phi_{jm}(x)\phi_{jn}(y) \in V_j, \tag{25}$$

where the 2D coefficients are denoted with capital letters: B_{jmn} and C_{jmn}. The corresponding wavelet space W_j is spanned collectively by the three types of basis functions,

$$\phi_{jm}(x)\psi_{jn}(y), \qquad \psi_{jm}(x)\phi_{jn}(y), \quad \text{and} \quad \psi_{jm}(x)\psi_{jn}(y),$$

which can be referred to as the "horizontal," "vertical,"

and ''diagonal'' wavelets, respectively, because of their sensitivity to (2D) patterns of stripes with the named orientations (Daubechies 1992). Denoting the respective wavelet coefficients as D^H_{mn}, D^V_{mn}, and D^D_{mn}, we then have the expansion

$$u'_j(x, y) = \sum_m \sum_n D^H_{jmn}\phi_{jm}(x)\psi_{jn}(y) + D^V_{jmn}\psi_{jm}(x)\phi_{jn}(y) + D^D_{jmn}\psi_{jm}(x)\psi_{jn}(y) \in W_j \quad (26)$$

for the 2D scale-difference signal.

Because the basis functions are tensor products of the 1D counterparts, the computational procedures for the 1D coefficients tend to be directly applicable. It is analogous to achieving a 2D discrete Fourier transform with a series of 1D transforms. For example, upscale projection of the B-spline coefficients can be performed by applying (18) along each index m and then along each n.

Of interest here is relating the 2D wavelet energy to the 1D energy profiles $\overline{(d_j)^2}$. The narrow scatterometer swaths (Fig. 1) allow reliable estimation of energy profiles only in the 1D along-track directions; however, the wind components must be synthesized over the North Atlantic basin using the energy statistics of the 2D wavelets. We assume statistical isotropy (Freilich and Chelton 1986) so that the 1D energy profiles $\overline{(d_j)^2}$ computed along lines parallel to the x and y axes are identical. Then by fixing y to be a constant, cross-sectional scale differences can be obtained by collecting terms involving $\psi_{jm}(x)$ from (26) as

$$u'_j(x) = \sum_m \left[\sum_n D^V_{jmn}\phi_{jn}(y) + \sum_n D^D_{jmn}\psi_{jn}(y)\right]\psi_{jm}(x), = \sum_m d_{jm}(y)\psi_{jm}(x),$$

from which the cross-sectional wavelet coefficients can be obtained as the terms in square brackets. Taking the average of these 1D coefficients over m as

$$d_j(y) = \sum_n D^V_{jn}\phi_{jn}(y) + \sum_n D^D_{jn}\psi_{jn}(y)$$

and then computing the square averages along y as in (15), noting orthogonality between ϕ and ψ, would yield

$$\overline{(D^V_j)^2} + \overline{(D^D_j)^2} = 2^{-j}\overline{(d_j)^2}. \quad (27)$$

Similarly, computing the wavelet energy profile along a fixed x would yield

$$\overline{(D^H_j)^2} + \overline{(D^D_j)^2} = 2^{-j}\overline{(d_j)^2}. \quad (28)$$

Although (27) and (28) imply $\overline{(D^H_j)^2} = \overline{(D^V_j)^2}$ (consistent with the isotropic assumption), distribution of the 1D energy profile between the diagonal and horizontal or vertical portions is difficult to infer without further information or assumption. An assumption of identical distribution then leads to

$$\overline{(D^H_j)^2} = \overline{(D^V_j)^2} = \overline{(D^D_j)^2} = 2^{-(j+1)}\overline{(d_j)^2}, \quad (29)$$

which is quite adequate for the purpose of synthesizing geometrically unbiased fields (i.e., no dominating patterns of stripes).

4. Scale-dependent statistics of the scatterometer data

Freilich and Chelton (1986) have studied spectral characteristics of an earlier scatterometer wind dataset from the Seasat-A satellite. Because of the relatively narrow (approximately 500 km) satellite swath, they avoided direct calculation of full 2D spectra and instead computed 1D spectra along the swath and inferred the 2D properties under isotropy and incompressibility assumptions. Our multiresolution analysis of the *ERS-1* satellite scatterometer follows an analogous approach employing along-track computations in conjunction with isotropic assumptions.

We have collected about 50 tracks each from the four ''seasonal'' months of July 1992, October 1992, January 1993, and April 1993. Only those tracks spanning at least half the latitudes of the North Atlantic domain (21°, Fig. 1) were considered. For each track, the 2D coefficients B_{jmn} were computed (appendix B) over the satellite swath at the resolution of $j = 2$ ($\Delta_2 = 27.8$ km) for both wind vector components. The resulting analytic fields, given by (24), were then sampled alongtrack at the midpoint of the swath at the interval of Δ_2. These alongtrack samples were in turn splined to produce a set of one-dimensionally supported wind data $[\hat{u}_j(y'), \hat{v}_j(y')]$, $y' \in [0, L]$, for each j, $-3 \le j \le 2$. The alongtrack scale-difference signals $u'_j(y')$ and $v'_j(y')$ for the resolutions of $j = -3, -2, -1, 0$ were then computed from (3). This particular set of resolutions covers the high-wavenumber band of our interest; the coarsest scale of analysis, $\Delta_{-3} \approx 900$ km, corresponds to the expected maximum wavenumber in the ECMWF analysis data at which a $\gamma \approx 2$ power law is observed, while the finest scale, $\Delta_0 = 111.2$ km, approaches the Nyquist limit for the alongtrack *ERS-1* scatterometer sampling interval.

a. Seasonal variances and power-law exponents

The first and second moments of the scale differences are computed along y' from each of the four *seasonal ensembles* of the tracks. As expected, the computed mean is zero

$$\overline{u'_j} = 0, \qquad \overline{v'_j} = 0 \quad (30)$$

for each j and each of the four months. The variances $\overline{(u'_j)^2}$ and $\overline{(v'_j)^2}$, plotted as standard deviations in Fig. 6, display a seasonal pattern of having higher values in ''winter/autumn'' than ''summer/spring,'' where the seasonal difference is more pronounced for lower-resolution (lower wavenumber) signals. It is difficult to infer from the available information whether or not the lack of seasonal variations at higher wavenumbers is a result of dominance by the measurement noise. Also,

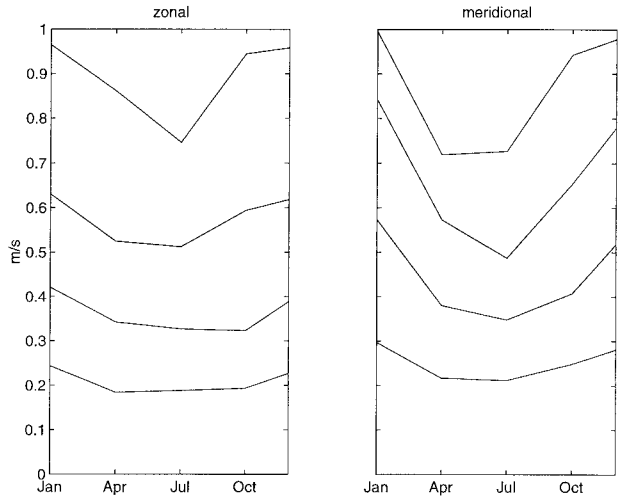

FIG. 6. The seasonal root-mean-squares (square roots of the variances) of the zonal and meridional scale differences $u_j'(y)$ and $v_j'(y)$ for the resolutions of, from top to bottom lines, $j = -3, -2, -1, 0$ (i.e., for the respective scales of 889.6, 444.8, 222.4, and 111.2 km). The four seasonal data points were linearly interpolated over the annual axes shown.

the lower-resolution scale differences have larger magnitudes than those of higher resolution, which is in agreement with the fractal energy models of the wind. Spectral energy densities have been estimated by (23) from the multiresolution variances $[\overline{(u_j')^2}, \overline{(v_j')^2}]$ as well as by applying a conventional Fourier-based method[3] to $[\hat{u}_2(y'), \hat{v}_2(y')]$. These energy densities are plotted in Fig. 7, showing reasonable agreements between the two spectral estimation methods. The plots of energy density clearly indicate a power-law dependence in the spectra. The power-law exponents computed from both Fourier and wavelet spectra by least square fits are given in Table 1 along with standard deviations for each "season." These exponent values are generally in good agreement with the corresponding midlatitudinal values (2.31 zonal, 2.11 meridional) observed by Freilich and Chelton (1986) in the Seasat data from the summer of 1978 over the Pacific. The fidelity of the estimated exponents, as measured by the smaller standard deviations,

[3] Welch's averaged periodogram with the Hanning window and FFT length of 256 is used.

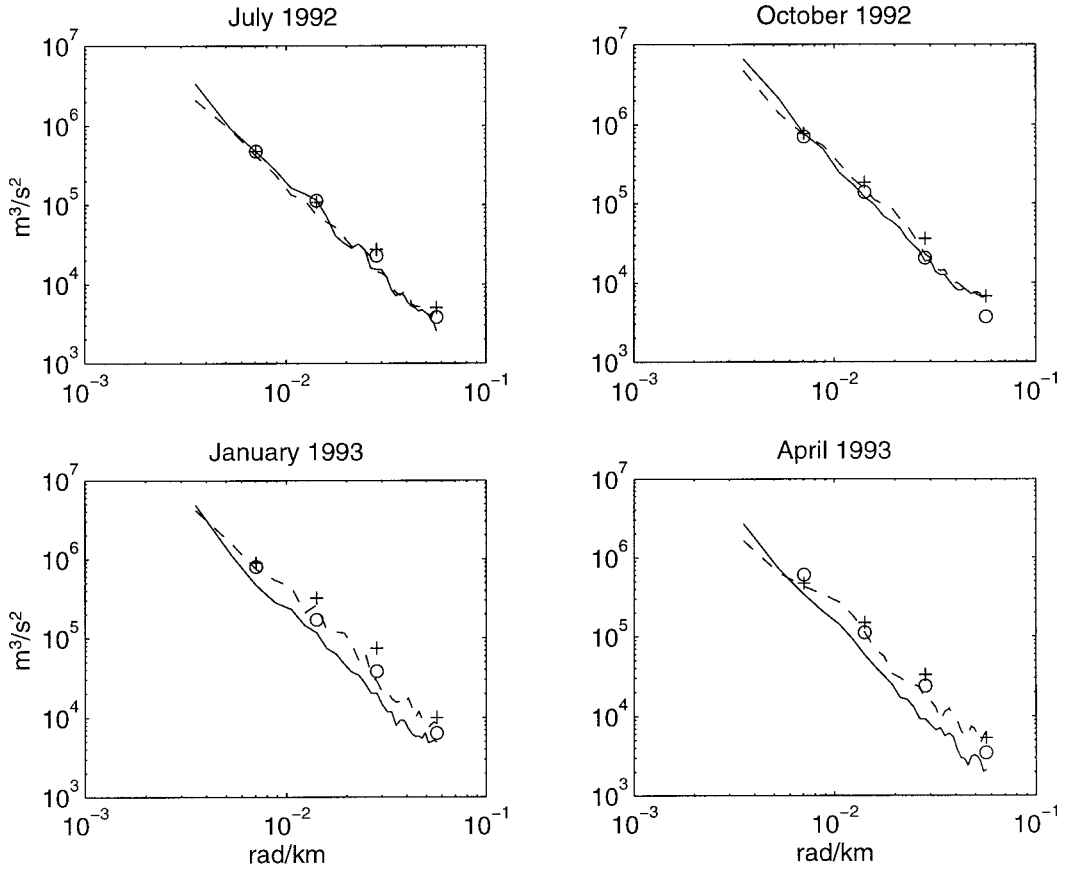

FIG. 7. Spectral energy densities computed from alongtrack samples of the scatterometer measurements of wind vector components. The solid and dashed lines are the Fourier spectra of the zonal (u) and meridional (v) components, respectively. The corresponding wavelet spectra are marked by "○" and "+," respectively.

TABLE 1. The power-law exponents γ computed from along track samples of the scatterometer measurements of wind vector components (u, v), using Fourier-based and wavelet-based methods. The high-wavenumber range of 0.007 to 0.06 rad km^{-1} (1/8 to 1 cycle per degree) is considered.

	Zonal (u)		Meridional (v)	
	Fourier	Wavelet	Fourier	Wavelet
July 1992	2.35 ± 0.68	2.26 ± 0.51	2.10 ± 0.63	2.05 ± 0.53
October 1992	2.44 ± 0.63	2.43 ± 0.67	2.30 ± 0.65	2.20 ± 0.60
January 1993	2.42 ± 0.63	2.26 ± 0.58	2.23 ± 0.55	2.28 ± 0.71
April 1992	2.29 ± 0.53	2.49 ± 0.54	2.03 ± 0.62	2.03 ± 0.67
All data	2.38 ± 0.62	2.35 ± 0.58	2.17 ± 0.62	2.14 ± 0.64

is much higher in those reported by Freilich and Chelton, which might be attributed to differences in scatterometer sampling and instrumentation—the Seasat used a Ku-band (14.6 GHz) radar, while the *ERS-1* data were obtained from a C-band (5.3 GHz) radar.

The surface wind over the North Atlantic is generally more energetic over the winter months because of frequent storms. The ''seasonal'' differences in our power-law exponents are reflections of differences in $[\overline{(u_j')^2}, \overline{(v_j')^2}]$ mentioned earlier. That is, the signal energy is larger in winter/autumn than summer/spring for each scale, but the lower-resolution signals have proportionally larger annual variations than the higher-resolution signals. The power-law exponents are consequently larger (more rapidly decaying energy spectra) in the more energetic winter/autumn signals.

b. Distribution of the wavelet coefficients

Statistically, turbulent activity becomes increasingly intermittent as the scale decreases. Such intermittency in turbulence is reflected in the shape of the probability density function as having more pronounced ''tails'' than the Gaussian distribution (Yamada and Ohkitani 1991; Meneveau 1991). For the purpose of generating wind-forcing datasets, this deviation from the Gaussian distribution has technical effects in the statistical synthesis of the high-wavenumber components. In particular, computation of wind stress curl tends to be sensitive to localized intense activities, and it is desirable that the observed and synthesized distributions of the high-wavenumber wind components are alike.

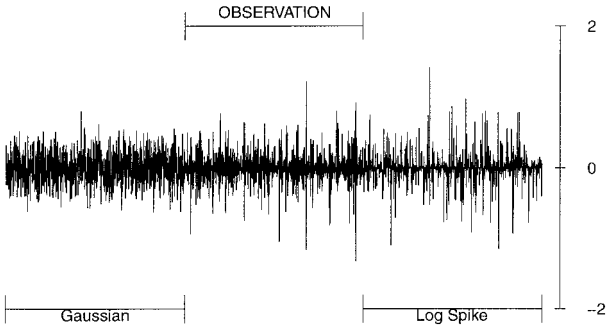

FIG. 8. Wavelet coefficients for the scatterometer data (middle third) along with samples of Gaussian (left third) and log spike (right third) distributions having the same variance as the wavelet coefficients. The wavelet resolution for the shown coefficients is $j = 0$, while the order of the log spike distribution is $n = 4$. The prominent spikes in the middle section are believed to be examples of intermittent large-magnitude events.

To observe scale-dependent distributions in the high-wavenumber range, we have computed using (14) the wavelet coefficients $d_{jm}, j = -3, \ldots, 0$, for the sampled, alongtrack *ERS-1* data $[\hat{u}_2(y'), \hat{v}_2(y')]$. The wavelet coefficients do indeed exhibit more intense activity than random samples synthesized from a Gaussian distribution with the identical mean (zero) and variance, as exemplified in Fig. 8. The figure also shows samples from a distribution with the density function

$$f(x) = \frac{1}{2a(n!)}\left(\log\frac{a}{|x|}\right)^n, \qquad -a \le x \le a \quad (31)$$

that appears to simulate the observed wavelet coefficient sets better by visual inspection, especially with respect to intermittent and intense activities. The probability density function (31) features a logarithmic spike at the mean value of $x = 0$, while the variance is given by the parameter a as $a^2/3^{n+1}$. Although this ''log spike'' distribution is bounded by the parameter a, the chances of sampling a value near the two extremes are higher than for the Gaussian counterpart. Also, as the order n of the density function increases, divergence from the Gaussian distribution becomes more pronounced. In particular, for a given value of variance, the bounding parameter a increases exponentially with the order n. For numerical generation of the log spike samples, the corresponding cumulative distribution function $F(z) \equiv \int_{-\infty}^{z} f(x)\,dx$, given as

$$F(z) = \begin{cases} 0, & z \le -a, \\ \dfrac{1}{2} + \dfrac{z}{2a}\displaystyle\sum_{k=0}^{n}\frac{1}{k!}\left(\log\frac{a}{|z|}\right)^k, & -a \le z \le a, \\ 1, & z \ge a, \end{cases} \quad (32)$$

can be useful in transforming the standard uniform distribution (yielding samples of $z \in [0, 1]$) to the log spike distribution [by, e.g., a piecewise linear approximation of the inverse $F^{-1}(z)$].

Normalized histograms of the wavelet coefficient

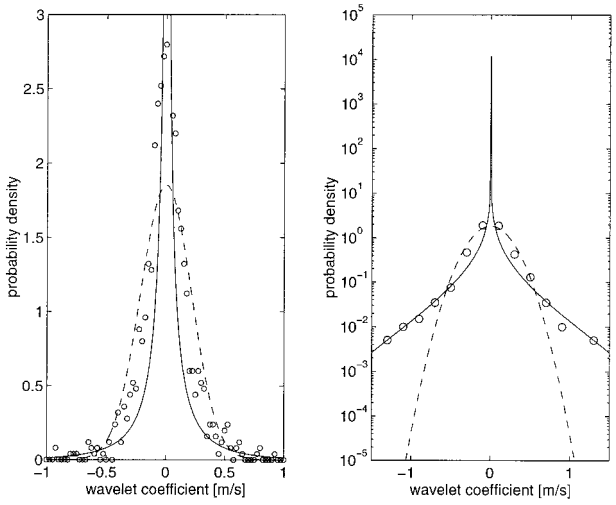

FIG. 9. Normalized histograms, marked with circles, of 1000 wavelet coefficients for the scatterometer data (at resolution of $j = 0$). The dashed and solid lines are, respectively, the Gaussian and log spike (order 4) probability density functions with the same variance as the shown coefficients. The right plot uses a logarithmic vertical axis for a better view of the ''tails.''

samples are compared with the Gaussian and log spike probability density functions. As depicted in Fig. 9, the larger tails of the log spike distributions can capture the intermittent events considerably better than the corresponding Gaussian distribution. As expected, deviation from the Gaussian distribution becomes more pronounced for the finer scales, as the order n of the best-fitting log spike distribution tends to increase with the resolution of wavelet. An order of 3 or higher is required to qualitatively fit the wavelet coefficient samples at the scale of Δ_0, while for the coarse scale of Δ_{-3}, an order of 1 or even the Gaussian distribution is adequate.

5. Composed wind fields

For comparison of ocean model responses, four sets of year-long, daily 2D wind fields $\mathbf{u} \equiv (u, v)$ are prepared by combining the ECMWF analyses with the *ERS-1* scatterometer data. Each of four composed wind sets contains distinct high-wavenumber content while sharing a common low-resolution dataset, as summarized in Table 2. The corresponding wind stress on the ocean surface can then be computed as

$$\boldsymbol{\tau} = \rho_a C_D |\mathbf{u}| \mathbf{u}, \tag{33}$$

where $|\mathbf{u}| \equiv (u^2 + v^2)^{1/2}$ is the wind speed, ρ_a is the air density at 1000-hPa temperature, and C_D is the neutral 10-m drag coefficient given by Large and Pond (1981). To force the ocean circulation model described in the next section, we have computed the wind stress curl, or the vertical component of the curl of $\boldsymbol{\tau}$ (neglecting the relatively small spatial derivatives of C_D),

$$\begin{aligned} \nabla_z \times \boldsymbol{\tau} &= \rho_a C_D \left[\frac{\partial}{\partial x}(|\mathbf{u}| v) - \frac{\partial}{\partial y}(|\mathbf{u}| u) \right], \\ &= \rho_a C_D \left\{ |\mathbf{u}| \left(\frac{\partial v}{\partial x} - \frac{\partial u}{\partial y} \right) + |\mathbf{u}|^{-1} \right. \\ &\qquad \left. \times \left[v^2 \frac{\partial v}{\partial x} - u^2 \frac{\partial u}{\partial y} + uv \left(\frac{\partial u}{\partial x} - \frac{\partial v}{\partial y} \right) \right] \right\}, \end{aligned} \tag{34}$$

over the ocean model grid of 1/5° × 1/6° for each of the four datasets. As mentioned previously, spline approximation (24) for each u and v allows analytic computation of the spatial derivatives in (34). Note that the expression inside the curly brackets in (34) would approach zero as the wind speed approaches zero.

a. Vector components and their energy spectra

The 2D B spline and BL wavelet are applied to the ECMWF and scatterometer datasets to obtain the vector components of wind fields in Table 2. The wind data for each day are processed independently. Also, each of the wind vector components (u, v) are processed separately and identically; thus, we only present the procedures applied to the u component for brevity.

The control or low-wavenumber wind dataset, referred to as the LO dataset hereafter, is obtained by applying a 2D cubic B spline to each of the daily (1200 UTC) ECMWF analysis fields. The resulting wind field is denoted as $u_{[LO]}(x, y)$ and computed as

TABLE 2. The four wind-forcing datasets.

LO	Low wavenumber Wind fields interpolated from the daily ECMWF analysis wind data.
HI-Sub	High wavenumber, by substitution of scatterometer data The LO fields regionally substituted by the daily (GMT) composite of the *ERS-1* scatterometer data.
HI-Bln	High wavenumber, blending of satellite swaths The HI-Sub fields statistically and regionally (off-swath only) augmented to blend away the satellite swaths evident in HI-Sub. The wavenumber augmentation is based on spectral statistics measured from the scatterometer data.
HI-stat	High wavenumber, purely statistical The LO fields augmented statistically as in HI-Bln but over the whole basin instead of regionally. No actual scatterometer data are incorporated.

$$u_{[\mathrm{LO}]}(x, y) = [\hat{u}_0(x, y)]_{\mathrm{ECMWF}}, \quad (35)$$

where the subscript ''ECMWF'' on the right-hand side indicates the input dataset used to compute the spline coefficients (appendix B). The spline scale of $\Delta_0 = 111.2$ km ($j = 0$) is used to approximate the particular sampling interval (1° latitude–longitude) of the ECMWF dataset. Previous analysis (e.g., Milliff et al. 1996) of the ECMWF fields have shown their $\gamma \approx 2$ power law to hold only for wavenumbers up to 0.007 rad km^{-1} (900-km wavelength), corresponding to a spline resolution of $j = -3$. A similar result is shown by the 30-day average spectral energy density (from January 1993) of both LO wind components (Fig. 10, solid lines). It is possible, however, that the LO wind fields locally contain some high-wavenumber variance not reflected in the basinwide Fourier energy spectra of Fig. 10 because both the ECMWF dataset and the B splines are capable of resolving higher wavenumbers.

The heterogeneous partial coverage of the scatterometer winds (Fig. 1) leads to three high-wavenumber counterparts to the LO wind dataset. The first is akin to that employed by Barnier et al. (1994) and is referred to as the HI-Sub dataset. It is obtained by substituting the daily scatterometer data into the background LO fields along the *ERS-1* orbital swaths. The HI-Sub wind component fields were computed as

$$u_{[\mathrm{HI\text{-}Sub}]}(x, y) = u_{[\mathrm{LO}]}(x, y) + [\hat{u}_2(x, y)]_{\mathrm{ERS1\cdot var}}, \quad (36)$$

where the spline dataset ''ERS1$\cdot$var'' for the second term on the right-hand side is the high-wavenumber variability signal extracted from the scatterometer observation. Specifically, if we let $(\tilde{x}, \tilde{y}, \tilde{u})$ be a data point in the scatterometer observation set, the corresponding ERS1$\cdot$var data point is $(\tilde{x}, \tilde{y}, \tilde{u}')$, where $\tilde{u}' \equiv \tilde{u} - u_{[\mathrm{LO}]}(\tilde{x}, \tilde{y})$ is an ECMWF-detrended version of the *ERS-1* observation. The cross-track resolution of the *ERS-1* data is 25 km, so the spline resolution is set at $j = 2$, or at a scale of $\Delta_2 = 27.8$ km. The variational spline analysis method described in appendix B is particularly useful for the irregularly sampled scatterometer data because the data-sparse regions are handled appropriately (splined to be zero) in a robust manner, maintaining fidelity in the low-wavenumber background field, even in the regions away from the satellite swaths. The spline also smoothly tapers the edges along the satellite swaths, reducing effects of discontinuity. Figure 11 (first and second panels) shows examples of meridional wind component fields and the associated wind stress curl fields for both the LO and HI-Sub datasets. It is evident that the scatterometer dataset increases finescale information, especially in the curl field. As expected, spatially heterogeneous composition of the high-resolution features in the HI-Sub data is also quite evident in Fig. 11, as the satellite tracks can be identified clearly in the curl field. Despite the highly heterogeneous spatial coverage, this enhancement by the scatterometer dataset restores much of the expected $\gamma \approx 2$ power-law spectral

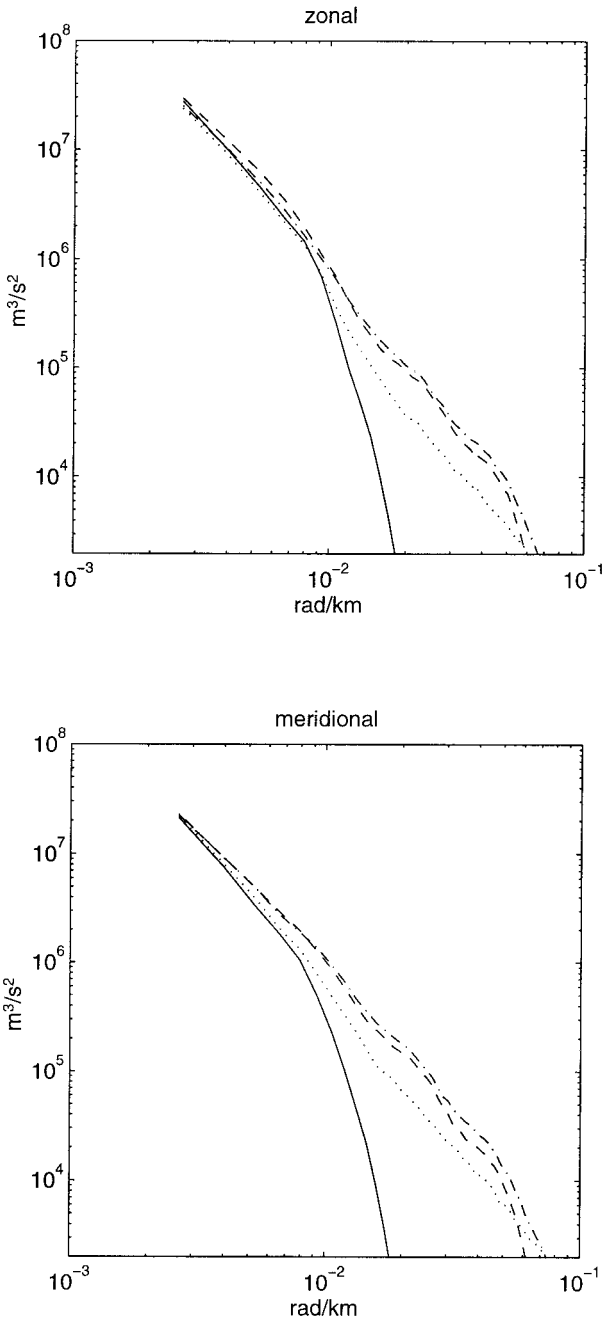

FIG. 10. The spectral energy densities of the wind vector components (u, v) for each of the four wind datasets (Table 2). Solid lines represent LO, dotted line HI-Sub, dash–dot line HI-Bln, and dashed line HI-stat.

characteristics, as indicated by the dotted lines of Fig. 10. These energy spectra of the HI-Sub set deviate from the expected power law only in the wavenumber range of approximately 0.007–0.014 rad km^{-1}, or a wavelength range of 900–450 km. Above and below this wavenumber range, the power-law relationship holds. An apparent effect of the heterogeneous sampling patterns of the scatterometer data to spectral density is a

range-specific (900–450-km wavelengths) energy dissipation.

The second high-wavenumber wind dataset is referred to as HI-Bln. It represents a successful attempt (Fig. 11, third panels) to reduce the artificial heterogeneity in high-wavenumber variance by using high-wavenumber synthesis off the satellite orbital swaths. The synthetic information could lead to improved ocean model performance if it truly reflects key statistics of the actual wind fields. Statistical synthesis is a viable technique here because full fields of (u, v) at the spatial resolutions of interest are currently available neither from measurements nor weather forecast analyses. The HI-Bln wind component fields were calculated from

$$u_{[\text{HI-Bln}]}(x, y) = \begin{cases} u_{[\text{HI-Sub}]}(x, y), \\ \quad \text{under satellite swaths,} \\ u_{[\text{LO}]}(x, y) + \sum_{j=-3}^{0} [u_j'(x, y)]_{\text{ERS1}\cdot\text{spect}}, \\ \quad \text{off swath,} \end{cases} \tag{37}$$

where the subscript ''ERS1 · spect'' indicates that the difference signals $u_j'(x, y)$ have been obtained from (26) using 2D wavelet coefficients, generated statistically, based on wavelet spectra of the seasonal *ERS-1* data. The high-wavenumber resolution range of $j = -3$ to 0 spans 900–100-km scales. The seasonal alongtrack wavelet energy values $\overline{(u_j')^2}$ were linearly interpolated, as indicated in Fig. 6, to yield monthly estimates of $\overline{(d_j)^2}$ using (16), which in turn allows estimation of the 2D wavelet coefficient variances $\overline{(D_j^H)^2}$, $\overline{(D_j^V)^2}$, $\overline{(D_j^D)^2}$ using (29). By construction, the means of the wavelet coefficients are zero. The log spike distribution (31) of order 3 was used to generate the coefficient samples. The spectral energy density of the resulting HI-Bln wind fields achieves a $\gamma \approx 2$ power-law relationship, as shown in Fig. 10 (dash–dot lines). The small ripples on the spectral energy plots are caused by the inherent wavenumber quantization of the orthonormal wavelet analysis as predicted by Wornell (1993). The meridional component and wind stress curl fields (Fig. 11, third panels) show no visible indication of satellite swaths. Note that the high-resolution signatures of the scatterometer measurements visible in HI-Sub are duplicated in HI-Bln, even though in the latter the patterns over the satellite swaths are blended well with the statistically generated wind components in the off-track gaps.

Finally, we have also prepared a fourth dataset generated by augmentation of the LO dataset with basinwide, purely statistical, high-wavenumber wind components. This dataset, referred to as HI-stat and shown in the fourth panels of Fig. 11, contains no actual scatterometer measurements (reflecting only their statistical information) along the satellite swaths. The wind component fields in this dataset were generated as

$$u_{[\text{HI-stat}]}(x, y) = u_{[\text{LO}]}(x, y) + \sum_{j=-3}^{0} [u_j'(x, y)]_{\text{ERS1}\cdot\text{spect}} \tag{38}$$

over the whole basin. Their energy density spectra, the dashed lines in Fig. 10, attain a $\gamma \approx 2$ power law, as in the case with the HI-Bln set.

b. Average curls of wind stress

The energy density spectra of the wind stress curl fields tend to be flatter than the wind component spectra, as expected from high-pass spectral characteristics of differential operators such as those in (34). The curl spectra for the scatterometer-enhanced HI-Sub and HI-Bln sets, shown in Fig. 12 as dotted and dash–dot lines, respectively, display this flatness over the entire high-wavenumber range, from 0.007 to 0.06 rad km^{-1} (wavelengths of about 100–900 km). The curl spectrum for the HI-stat set (dashed line) with purely statistical spectral enhancement is, however, significantly steeper in this high-wavenumber range, suggesting that the first- and second-order statistics under a *homogeneity* (basinwide) assumption are not sufficient to capture realistic high-wavenumber wind stress curl characteristics.

Figure 12 indicates that the *ERS-1* wind stress curl spectra do not obey a single power law, which is in agreement with an earlier analysis by Freilich and Pazdalski (1995). Comparing the curl spectra of LO and HI-stat sets in the figure, it is also evident that spectral enhancement of wind vector components in the specific wavenumber range of 0.007–0.06 rad km^{-1} has increased the energy density of the wind stress curl over a much wider wavenumber range, especially in the low wavenumbers. Such cross-wavenumber enhancing effects are exaggerated by incorporation of the scatterometer data, as indicated by the HI-Sub and HI-Bln curl spectra (in comparison to the LO curl spectrum). A likely cause is the nonlinear relation (34) between the surface wind vector components and wind stress curl.

It would be possible to synthesize wind component fields whose wind stress curl has a spectral characteristic similar to those with the scatterometer data, using spatially homogeneous statistics as in the construction of the HI-stat set. First, components at finer scales (e.g., Δ_1) than the upper bound of the high-wavenumber range must be synthesized. The curl energy in the high wavenumber would then be enhanced by the cross-wavenumber effects just described. Second, the synthesis at all scales must be performed with exaggerated intermittency (e.g., by using a higher-order log spike distribution) than observed, to obtain the effects of heterogeneity. We have not pursued such ad hoc approaches in order to adhere to the actual statistical observations of the scatterometer data. We also feel that the wind vector components have better established spectral characteristics through the power laws, upon which a more robust composition scheme can be designed.

6. Ocean model responses

Each of the four wind datasets (Table 2) are used to drive a general circulation scale calculation of the North

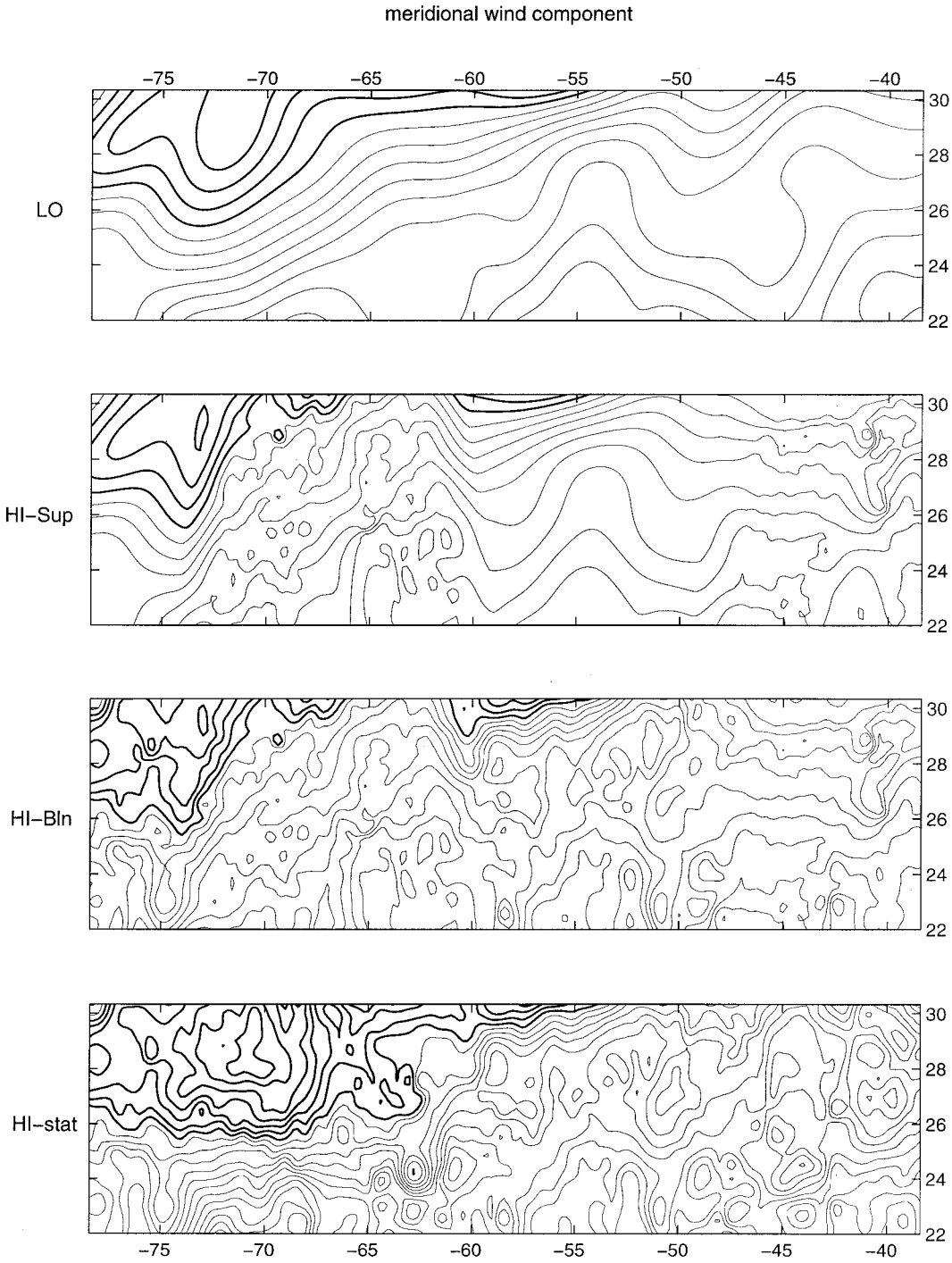

FIG. 11. (a) Fields of meridional wind component and (b) wind stress curl over a 40° × 8.5° region for the four wind datasets (Table 2). Contour intervals are 1 m s^{-1} for the wind component and 3×10^{-7} N m^{-3} for the wind stress curl. The thicker contour lines represent contours of northward wind components and positive curl (including the zero contour lines), while thinner lines represent southward wind and negative curl. The horizontal and vertical axes are longitudes and latitudes, respectively.

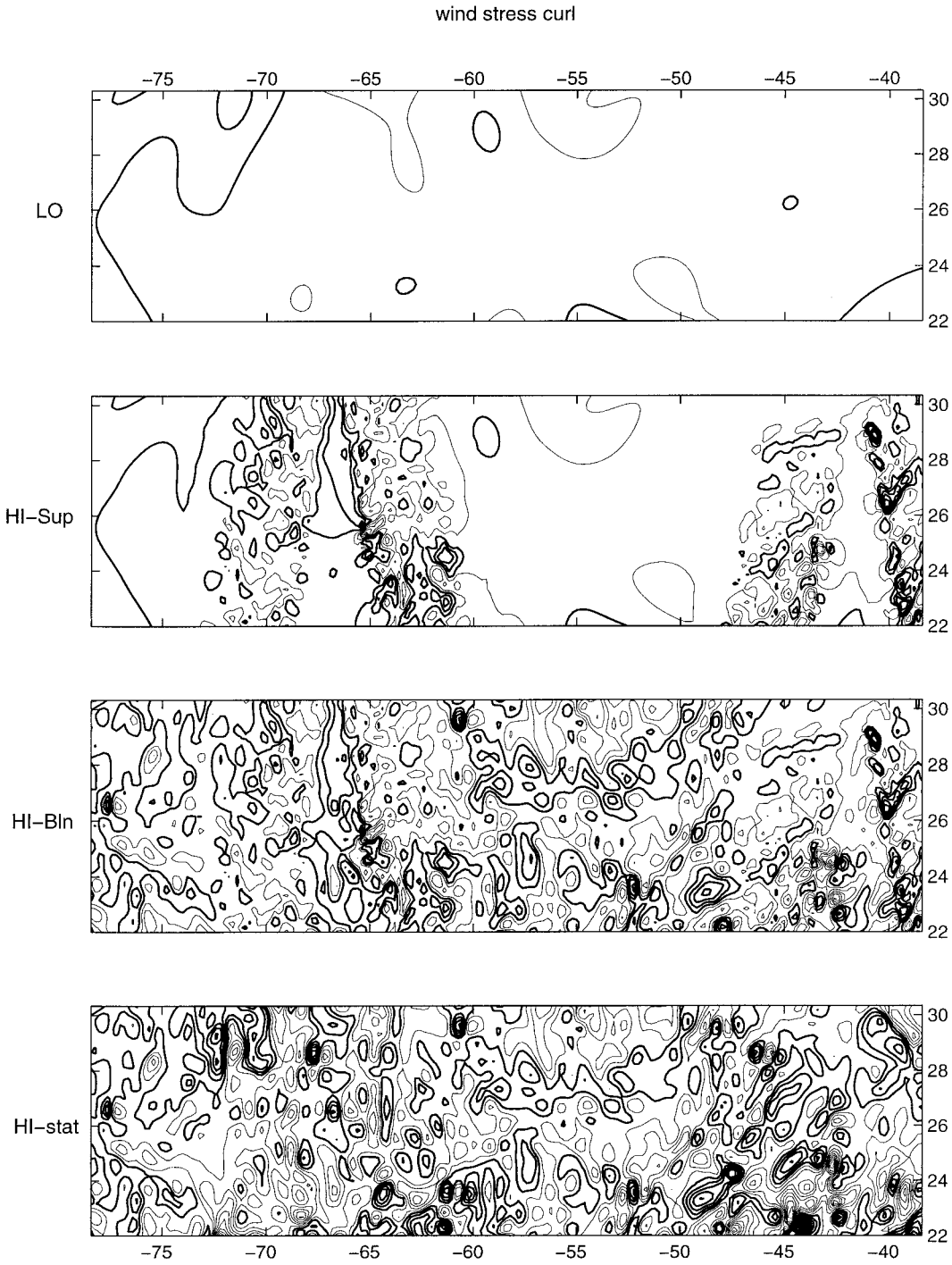

FIG. 11. (*Continued*)

Atlantic Ocean. The ocean model and experimental design are taken from Milliff et al. (1996). In that work, the general circulation response of a high-resolution (1/5° × 1/6°), five-level, quasigeostrophic model was studied as a function of controlled wavenumber content in the wind stress curl forcing fields. In the absence of coincident scatterometer observations, the high-wavenumber forcing in Milliff et al. (1996) was synthesized, via a global Fourier method, from smoothed representations of the ECMWF analyses according to a $\gamma = 2$ power-law dependence. (No high-resolution wind observations were used to control the synthesis in the previous study.) As before, the ocean model initial fields in the present study are identical for each of the four

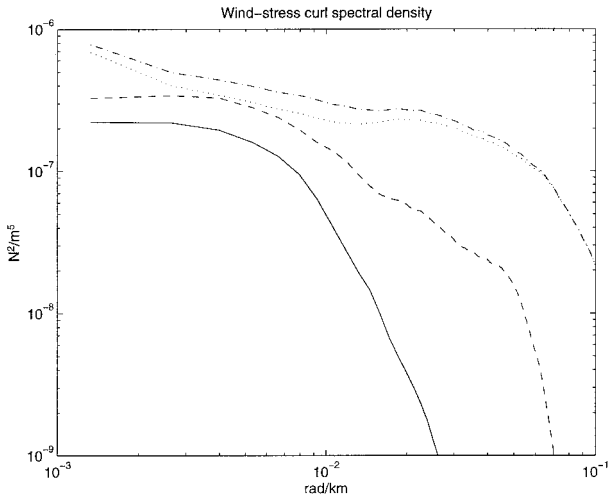

FIG. 12. The spectral energy densities of the wind stress curl for each of the four wind datasets (Table 2). Solid lines represent LO, dotted line HI-Sub, dash–dot line HI-Bln, and dashed line HI-stat.

calculations performed. Each wind-forcing dataset is then used to drive a 20-yr calculation in a repeating annual cycle mode (the wind stress curl fields for each dataset are blended smoothly between the final 10 days of June 1993 and the first 10 days of July 1992). Average circulation and basin-average energetics are computed using the final 5 years of integration for each experiment.

In the previous study by Milliff et al. (1996), the ocean model general circulation response to high-wavenumber content in the forcing exhibited improved energetics (eddy and mean kinetic energy fields) and patterns of circulation in the upper ocean. The circulation pattern of the Azores Current (18°–34°N, 40°–20°W) in the eastern basin was more like the observed climatology when the forcing fields contained realistic variance on horizontal scales of 4°–8°. The dynamics of the improved response were demonstrated to be essentially linear, such that differences in the annual average wind-forcing fields (Fig. 13) are informative. We should expect enhancements in the ocean model general circulation driven by the new datasets to be consistent with the previous results driven by synthetic high-wavenumber winds. We will compare among the four wind-forcing datasets the annual average wind stress curl fields and upper-ocean streamfunction responses. In addition we will examine basin-integrated measures of eddy and mean kinetic energies (EKE and MKE, respectively).

In contrast to Milliff et al. (1996), the LO wind-forcing dataset in the present study is taken directly from the ECMWF analyses. The high-wavenumber cutoff is now neither a homogeneous function of space nor is it well known from region to region. The annual average wind stress curl for the LO wind-forcing dataset is shown in Fig. 13a, and the upper-ocean streamfunction response is in Fig. 14a. Figure 14a demonstrates that in the region of the Azores Current, the analysis fields contain sufficient power at wavenumbers corresponding to scales of 4°–8° (see also Fig. 2 in Milliff et al.) to affect improvements in the general circulation patterns noted above.

Figure 13b depicts the annual average wind stress curl for the HI-Sub dataset. The effect of scatterometer observations on the high-wavenumber content of the annual-average field is obvious (presence of finescale features) but is spread heterogeneously across the domain. For example, the structure of the positive wind stress curl signal offshore of Cape Hatteras (36°–44°N, 72°–50°W) in Fig. 13a is superposed in Fig. 13b by a population of high-amplitude, small-scale features of wind stress curl. Conversely, in the southwestern portion of the domain, large-scale positive (at 12°N, 76°W) and negative (at 19°N, 72°W) centers in Fig. 13a remain largely unaltered in Fig. 13b. Moreover in Fig. 13b, there are dominant patterns in the north-central and northeastern portions of the basin that are reminiscent of swath tracks from the sampling scheme of the *ERS-1* scatterometer. Figure 2 demonstrates that these signals are indeed artifacts that correspond to positions in the *ERS-1* orbit when the scatterometer instrument was turned off, presumably in favor of the synthetic aperture radar instrument that competed for onboard power.

These sampling artifacts in the northeastern basin persist in the annual average wind stress curl from the HI-Bln dataset as well. The ocean model responds (Figs. 14b and 14c) to this artifact, altering the circulation pattern in the North Atlantic Current region of the 5-yr average solutions. The local nature of the HI-Sub and HI-Bln syntheses cannot compensate for the large-scale artifacts in the inadequately sampled scatterometer data. However, this is not the case in Fig. 13d for the HI-stat dataset with spatially homogeneous high-wavenumber content. The average ocean model response (Fig. 14d) is characterized by increased (decreased) maxima (minima), and the hint of smaller spatial scales versus the average solution driven by the LO dataset.

The first row of Table 3 infers Gulf Stream transport, for each of the 5-yr average solutions, by estimating a (normal) derivative of the streamfunction, integrated in the vertical over the top two model levels (pycnocline to surface). The derivative is estimated between the same two grid locations offshore of the separation point. The synthesis techniques, emphasizing scatterometer observations that are local in space (HI-Sub and HI-Bln), decrease the average transport by about 10% relative to the LO case. The more global and statistically homogeneous method (HI-stat) increases the average Gulf Stream transport by only about 1%.

The basin-average, upper-ocean response in terms of kinetic energy (Table 3) demonstrates about a 5% decrease in HI-Sub and HI-Bln solutions relative to LO, and about an 8% increase in the HI-stat case. Similar tendencies, with slightly larger amplitudes, are evident for basin-average MKE, reflecting the energetics of the large-scale circulation patterns. However, the most marked effects occur for basin-average EKE that in-

creases as the high-wavenumber energy density of the forcing fields. The upper-level EKE response increases by 26%, 37%, and 20% for HI-Sub, HI-Bln, and HI-stat, respectively. These changes are reflecting model responses to wavenumbers greater than about 0.014 rad km^{-1} (or scales finer than 4°), where the LO dataset displays orders of magnitude less variance than the other three datasets (Fig. 12), and are comparable to similar measures described in Milliff et al. (1996).

7. Summary and discussion

Techniques of multiresolution analysis have been applied to create wind-forcing datasets that combine high-resolution, swath-based observations from a scatterometer with low-resolution, uniformly sampled analysis fields from operational weather centers. The particular daily wind fields presented here are based on all observational data assimilated into the ECMWF analysis fields—sea level pressure, winds, temperature and humidity at the surface and aloft, and satellite cloud and temperature sounding retrievals. The *ERS-1* scatterometer then provides a several-fold increase in resolution and quantity of surface wind observations incorporated into the daily wind fields.

The new methodology includes both local and global approaches that preserve either the actual scatterometer observations themselves or regional and temporal averages of their statistics. In our approach, the syntheses are additionally guided by spectral properties that derive from the theory of 2D turbulence and the existing observations of high-resolution surface winds over the ocean. Average ocean circulation simulations, driven by the wind fields created by the new techniques, are consistent with the previous experiments by Milliff et al. (1996), especially with respect to sensitivity of circulation patterns and eddy kinetic energies to the high-wavenumber forcing. The model responses are, therefore, not dependent on the particular techniques used to enhance the high-wavenumber components in the wind forcing. The model simulations also demonstrate the utility of the new methods for preparation of hybrid high-wavenumber wind datasets to force ocean general circulation models.

The multiresolution analysis technique with an orthonormal wavelet basis can perform the traditional Fourier-based spectral decomposition over a quantized wavenumber set. In particular, the wavelet and Fourier bases lead to consistent estimates of spectral energy densities and power-law dependencies, but the wavelet-based technique has an advantage of spatial specificity. This advantage is most significant during statistical synthesis of the high-wavenumber wind components between satellite swaths. It is also useful when the winds are not spatially stationary in the alongtrack direction. Generally, a wavelet-based technique is suitable for regionally dependent (i.e., spatially specific) spectral analysis. Annual composite averages of the high-wavenumber components of the scatterometer data do indeed display a spatially structured distribution over the North Atlantic domain. Such regional heterogeneity is exaggerated in wind stress curl fields (Fig. 13). Also, low-wavenumber energy in wind stress curl can be sensitive to an energy source in wind vector components at higher wavenumbers—a possible pathway by which high-wavenumber wind components affect large-scale ocean circulation. The log spike distribution function is an alternative to the Gaussian distribution for characterization and synthesis of processes exhibiting intermittency; however, characterization via statistical intermittency is not a substitute for determining regionally dependent statistics, especially to capture the spatial and spectral structures of the wind stress curl fields. The basinwide homogeneous statistics used in generation of the HI-Bln and HI-stat wind sets can thus be improved by introducing regional dependence. Studies on spatial heterogeneity of high-wavenumber statistics are currently under way.

The application of the new methodology to the North Atlantic provides a stringent test. Figure 2 demonstrates a sampling artifact in the northeastern part of the basin that introduces a strong bias in the observations. The *ERS-1* scatterometer instrument was turned off systematically such that the northeastern basin was rarely or never sampled, while regions of the western basin were frequently sampled. The step function character of the artifact is exacerbated in the production of wind stress curl fields that involve spatial derivatives normal to the feature. The sampling bias is not accounted for in the local method (i.e., HI-Bln) that has been developed here to perform statistical extension of the high-wavenumber signal, while preserving all high-resolution wind observations as they occur. Conversely, the more global method (i.e., HI-stat) is not sensitive to the bias, but it does not preserve measured high-resolution local patterns of the wind stress curl field. The HI-Bln method thus seems more applicable to regional and time-specific simulations, while the HI-stat method might be appropriate for studies of the energetics and climatology of the general circulation (Barnier et al. 1991; Milliff et al. 1996).

We emphasize that the HI-Bln and HI-stat methods are flexible enough to be made more regionally and temporally specific. The methodology presented in the paper provides numerical tools to introduce regional and temporal statistics in the analyzed wind fields. A remaining issue is to improve statistical characterization of the high-wavenumber wind components in terms of regional variability and temporal correlation through adequately sampled measurements. For example, regional statistics from the NSCAT scatterometer (Naderi et al. 1991), with a 1500-km swath width, might alleviate the sampling artifacts noted above. The wider swath also seems useful in relaxing the isotropic assumption (section 4), which might not be appropriate near coastlines.

Acknowledgments. We appreciate the support from NASA/JPL for the NSCAT Science Working Team at NCAR. We also thank Tim Hoar and Steve Worley (both

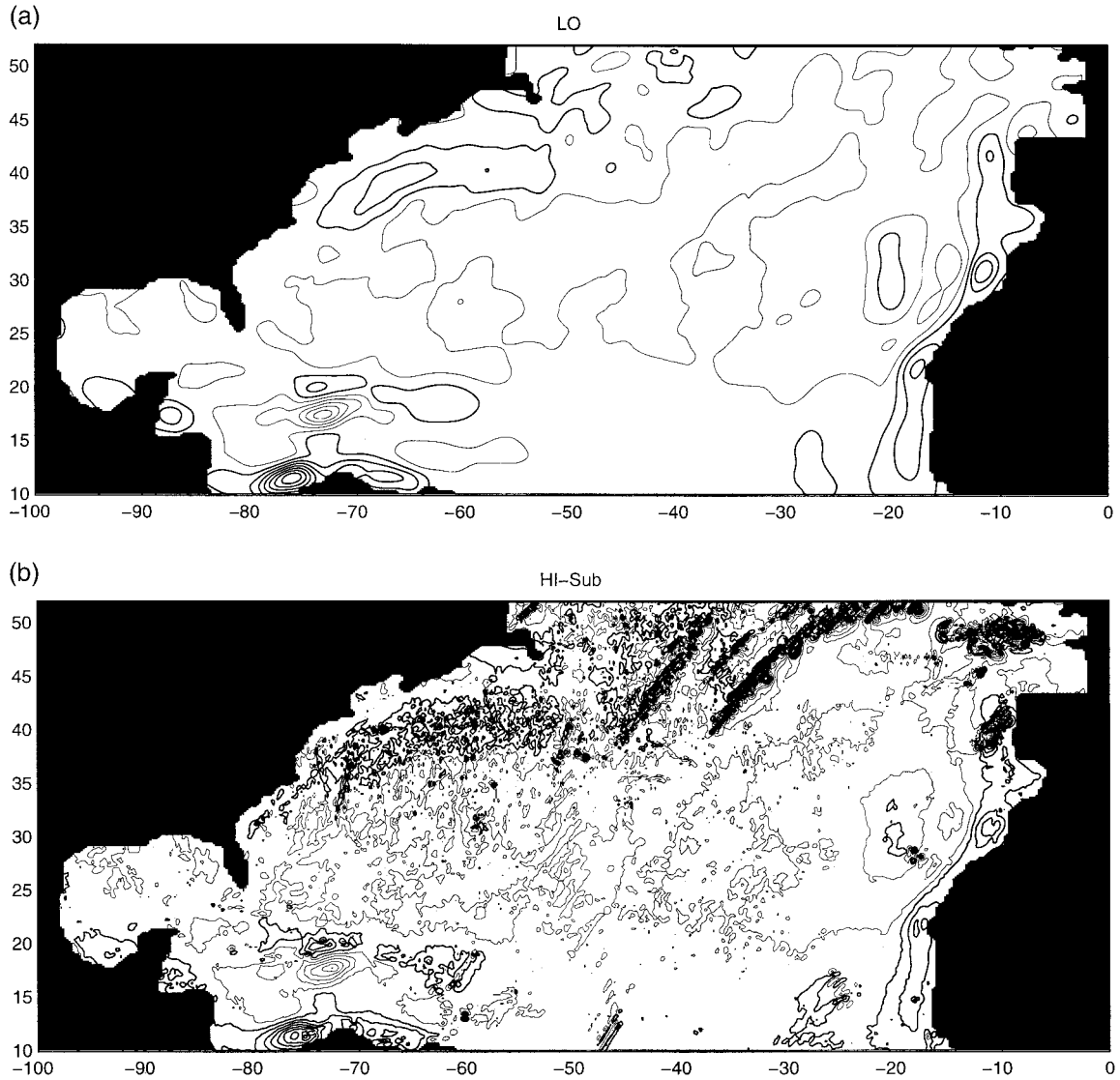

FIG. 13. The yearly average wind stress curl fields for (a) LO, (b) HI-Sub, (c) HI-Bln, and (d) HI-stat. The contour interval is 10^{-7} N m^{-3}. The thicker contour lines represent positive values (including zero).

at NCAR) for assistance in preparing the observation datasets. One author (T.M.C.) was jointly supported by the Geophysical Statistics Project (sponsored by NSF Grant DMS93-12686) and Advanced Study Program at NCAR. Funding by Office of Naval Research (Grant N00014-95-1-0257) is also appreciated.

APPENDIX A

Series Representations of Battle–Lemarié Wavelet Functions

An orthonormal basis for the wavelet spaces can be generated by scaling and translation of a single function called the wavelet function or the mother wavelet. In the B-spline multiresolution analysis, a standard wavelet function is the Battle–Lemarié wavelet function $\psi(x)$ that can be generated from the corresponding B-spline function as an infinite series,

$$\psi(x) = \sum_p g_p \beta(2x - p), \tag{A1}$$

which yields the orthonormal wavelet basis $\{\psi_{jm}(x)\}$ as

$$\psi_{jm}(x) = 2^{j/2}\psi\left(\frac{x}{\Delta_j} - m\right), \tag{A2}$$

$$= 2^{j/2} \sum_p g_p \beta\left(2\frac{x}{\Delta_j} - 2m - p\right), \tag{A3}$$

and

$$= \frac{1}{\sqrt{2}} \sum_p g_p \beta_{j+1,2m+p}(x) \tag{A4}$$

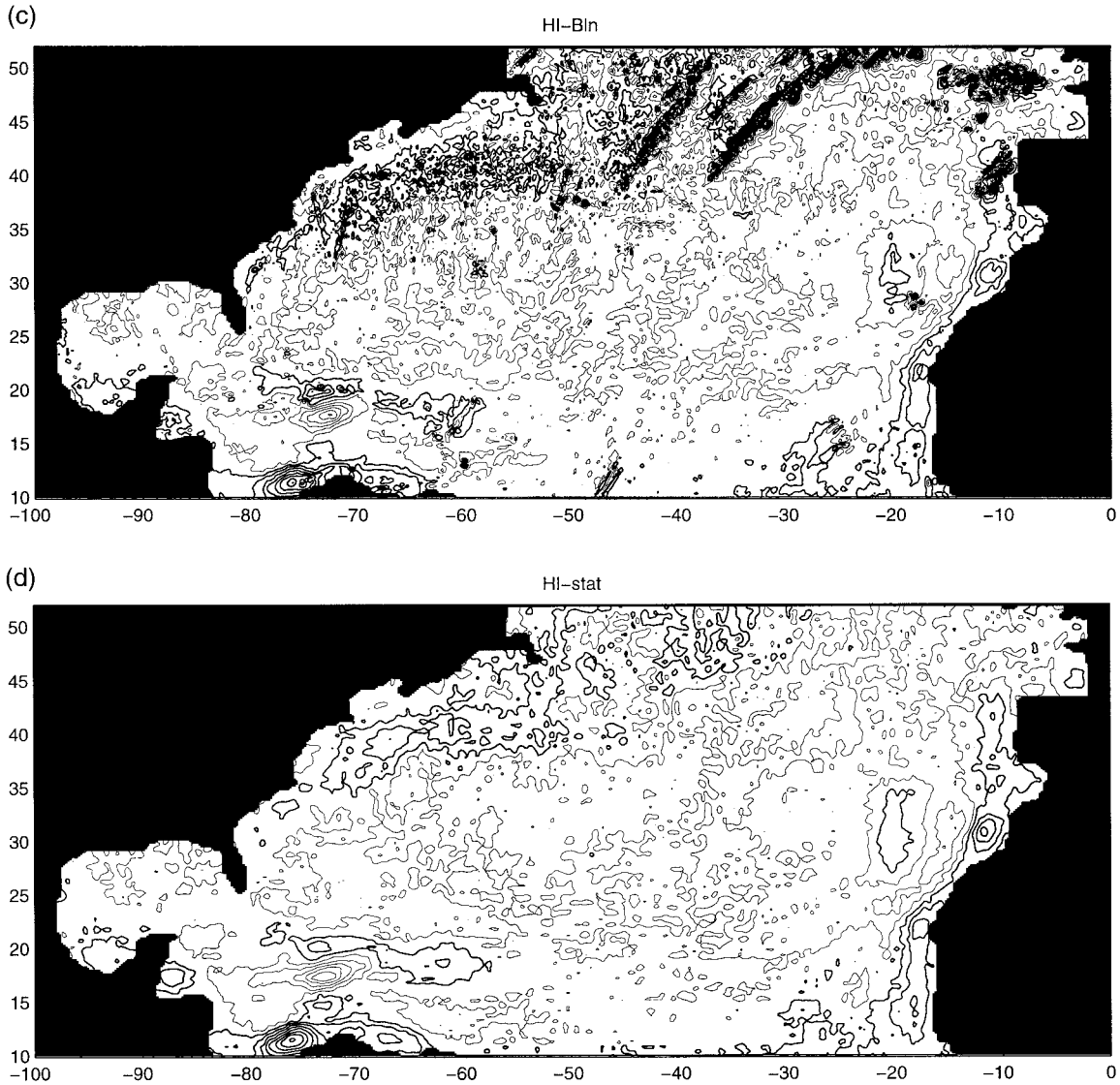

FIG. 13. (*Continued*)

for an order-dependent set of coefficients g_p. Table A1 lists the coefficients for the third-order polynomial wavelet (BL-3), used in conjunction with the cubic B-spline function (5).

Analogously, an orthonormal basis of the approximation spaces V_j can be generated by the accompanying Battle–Lemarié scaling function $\phi(x)$ (or the father wavelet) as

$$\phi(x) = \sum_p h_p^{\dagger} \beta(x - p) \tag{A5}$$

for given $h_p^{\dagger}$ (Table A1 for BL-3). This linear transformation (A5) is invertible; thus, the orthonormal basis $\{\phi_{jm}(x)\}$ spans the same approximation space V_j as the corresponding B-spline basis. Note the scaling of x by 2 in the right-hand side of (A1) but not in (A5). An expression closer to (A1) can be obtained by applying the dilation relation, such as (17) for the cubic polynomial case, to (A5)

$$\phi(x) = \sum_p h_p \beta(2x - p) \tag{A6}$$

for given h_p (Table A1 for BL-3). The orthonormal approximation (spline) basis $\{\phi_{jm}(x)\}$ can then be obtained as

$$\phi_{jm}(x) = \frac{1}{\sqrt{2}} \sum_p h_p \beta_{j+1,2m+p}(x). \tag{A7}$$

Using (A4) and (A7), the orthonormal expansions in the approximation and wavelet spaces V_j and W_j can both be expressed in terms of B-spline expansions in V_{j+1} as

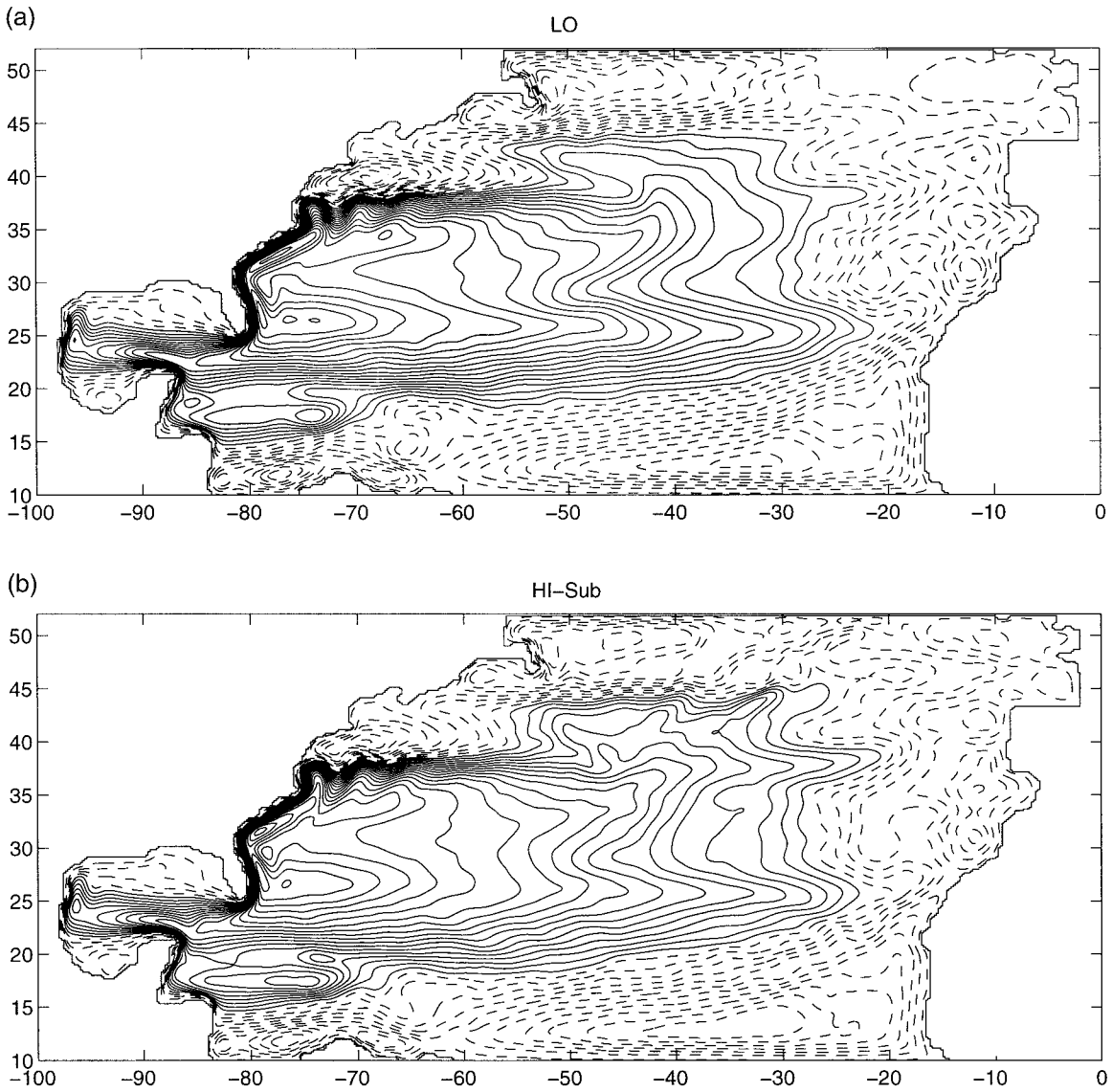

FIG. 14. The 5-yr average surface streamfunction outputs from the quasigeostrophic model forced by the (a) LO, (b) HI-Sub, (c) HI-Bln, and (d) HI-stat datasets. The contour interval is 2000 m^2s^{-1}. The solid (dashed)lines represent positive (negative) values.

$$\sum_{m'} c_{jm'}\phi_{jm'}(x) = \frac{1}{\sqrt{2}} \sum_{m} (c_j * h)_m \beta_{j+1,m}(x) \quad \text{(A8)}$$

$$\sum_{m'} d_{jm'}\psi_{jm'}(x) = \frac{1}{\sqrt{2}} \sum_{m} (d_j * g)_m \beta_{j+1,m}(x), \quad \text{(A9)}$$

where the asterisk (*) denotes a convolution-like operation defined as $(c_j * h)_m \equiv \Sigma_p\, c_{jp} h_{m-2p}$. These B-spline expansions are especially useful in synthesis using the multidimensional wavelet bases.

Although the sets of series coefficients $\{h_p\}$, $\{h_p^\dagger\}$, and $\{g_p\}$ are infinite, they are all decaying sequences (in magnitudes). Thus, (A1) and (A6) can be readily approximated by finite, truncated series. In particular, the first 11 values from Table A1 have been used for each of h_p and g_p to obtain the BL-3 wavelet and scaling functions depicted in Fig. 4.

APPENDIX B

Variational Computation of B-Spline Coefficients

This section presents a solution for the 2D spline problem (24). The simpler expressions for the corresponding 1D solution to (9) can be derived straightforwardly (by fixing the dimensional variable y and removing variations indexed by n and q).

Consider solving for the B-spline coefficients $\{B_{mn}\}$ in

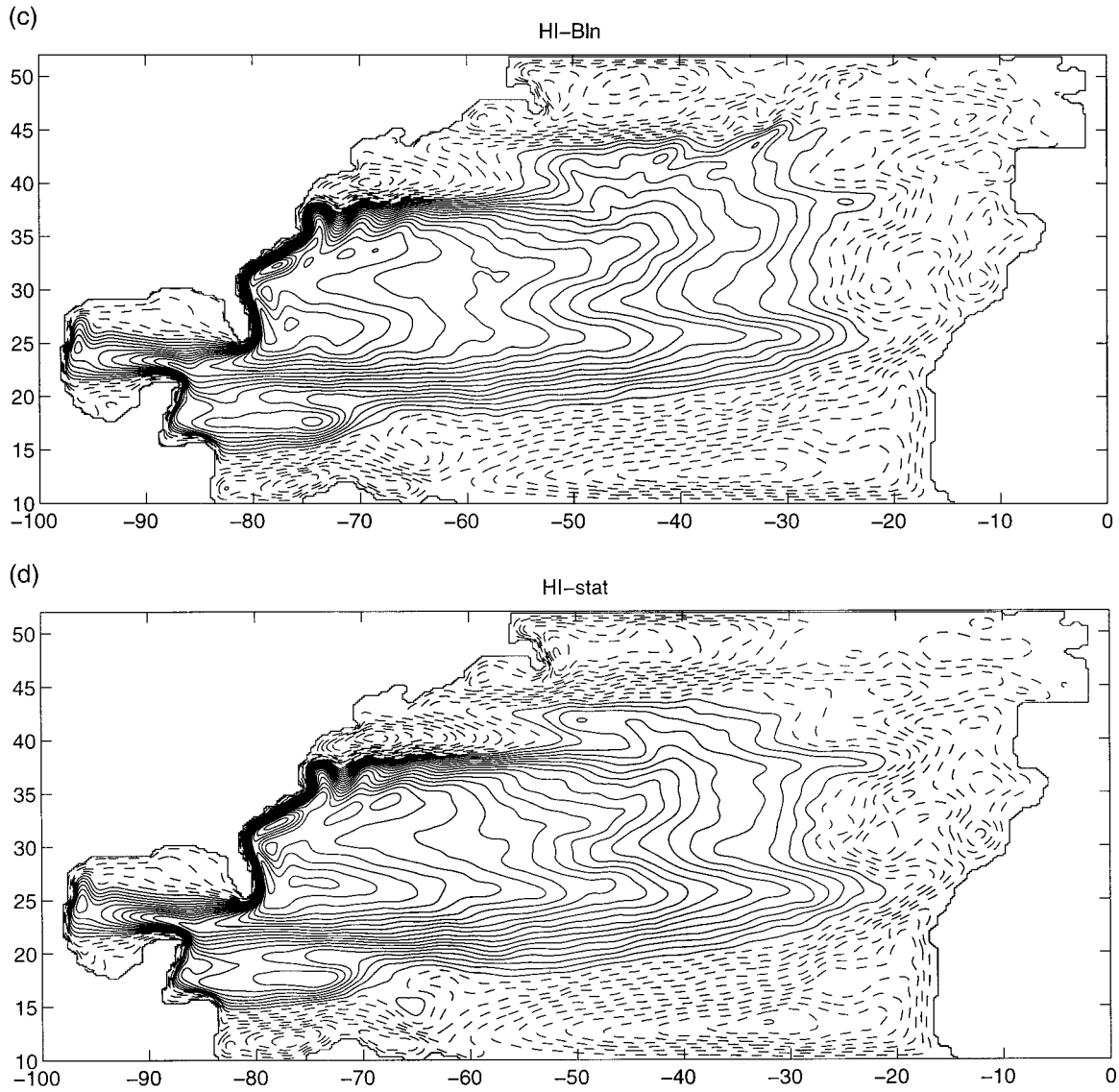

FIG. 14. (*Continued*)

TABLE 3. Selected quantities computed from the outputs of the model runs driven by the three wind datasets. KE, MKE, and EKE denote, respectively, the total, mean, and eddy kinetic energy. Subscripts for KE, MKE, and EKE represent model levels from shallow to deep. The ''Gulf Stream transport'' is computed from the streamfunction off shore from the separation point in the first two levels (above the pycnocline).

	LO	HI-Sub	HI-Bln	HI-stat
Gulf Stream transport [Sv]	24.75	22.22	22.98	25.08
KE_1 [10^6 (cm s^{-1})^2]	1.60	1.52	1.52	1.73
KE_{1+2} [10^6 (cm s^{-1})^2]	1.96	1.85	1.94	2.13
MKE_1 [10^6 (cm s^{-1})^2]	1.04	0.95	0.96	1.07
EKE_1 [10^6 (cm s^{-1})^2]	0.68	0.86	0.93	0.82
MKE_2 [10^6 (cm s^{-1})^2]	0.15	0.13	0.14	0.16
EKE_2 [10^6 (cm s^{-1})^2]	0.27	0.30	0.34	0.33
MKE_1/KE_1	64.7%	62.5%	63.1%	62.1%
EKE_1/KE_1	42.5%	56.8%	61.2%	47.3%
MKE_2/KE_{1+2}	7.4%	7.2%	7.4%	7.5%
EKE_2/KE_{1+2}	13.9%	16.1%	17.3%	15.5%

TABLE A1. The B-spline expansion coefficients (truncated sets) for the third-order Battle–Lemarié scaling and wavelet functions. Note that the wavelet coefficients g_p are shifted by one in index.

p	g_{p+1}	h_p	$h_p^\dagger$
0	2.8917341102	1.3092136400	1.9697616818
±1	−2.0052105784	0.6486655983	−0.6724304853
±2	0.5422790147	−0.2245146233	0.2687042436
±3	−0.0120714056	−0.2018631209	−0.1185199448
±4	0.1440886662	0.1026593789	0.0551914644
±5	−0.1459124924	0.0750921494	−0.0265203391
±6	0.0030183628	−0.0484029951	0.0129981659
±7	0.0283439282	−0.0316642402	−0.0064574918
±8	0.0191492593	0.0232635628	0.0032398631
±9	−0.0224619831	0.0143355627	−0.0016377760
±10	−0.0049649034	−0.0113665505	0.0008328361
±11	0.0083303250	−0.0067610866	−0.0004255524
±12	0.0038529062	0.0056263956	0.0002183103
±13	−0.0047050427	0.0032703371	−0.0001123697
±14	−0.0016375943	−0.0028133652	0.0000580049
±15	0.0021567614	−0.0016088144	−0.0000300159
±16	0.0009314220	0.0014179888	0.0000155658
±17	−0.0011244360	0.0008010435	−0.0000080875
±18	−0.0004545335	−0.0007192446	0.0000042091
±19	0.0005541175	−0.0004024699	−0.0000021939
±20	0.0002408389	0.0003667111	0.0000011450
±21	−0.0002844463	0.0002036419	−0.0000005984
±22	−0.0001225537	−0.0001877710	0.0000003130
±23	0.0001440664	−0.0001036210	−0.0000001639
±24	0.0000639078	0.0000964925	0.0000000859
±25	−0.0000740140	0.0000529703	−0.0000000451
±26	−0.0000329938	−0.0000497379	0.0000000237
±27	0.0000379572	−0.0000271824	−0.0000000124
±28	0.0000171718	0.0000257055	0.0000000065
±29	−0.0000195819	0.0000139945	−0.0000000034
±30	−0.0000089218	−0.0000133156	0.0000000018

$$\hat{u}(x, y) = \sum_{m=1}^{M} \sum_{n=1}^{N} B_{mn}\beta(x - m)\beta(y - n), \quad \text{(B1)}$$

given the measurements of the unknown field $u(x, y)$ and their observational positions denoted as $\tilde{u}_k$, $\tilde{x}_k$, and $\tilde{y}_k$, respectively, for $k = 1, 2, \ldots, K$. The resolution parameter j is assumed given and fixed throughout this section and hence is dropped for brevity in notations. Without loss of generality, the origin of the coordinates (x, y) is selected (e.g., at near the lower-left corner of the analysis domain) so that the translation parameters can take on the values of $m = 1, 2, \ldots, M$ and $n = 1, 2, \ldots, N$. The goal is to find a continuous approximation $\hat{u}(x, y)$ that minimizes the approximation error

$$\mathcal{S}(u) \equiv \sum_{k=1}^{K} \tilde{w}_k^d \|u(\tilde{x}_k, \tilde{y}_k) - \tilde{u}_k\|^2, \quad \text{(B2)}$$

where $\tilde{w}_k^d$ is the data weight representing relative confidence in the data and reflecting measurement noise variance. (A formulation incorporating correlations among the measurement noise processes can be obtained as a straightforward extension.)

Variational approach to spline is especially useful in dealing with datasets with irregular sampling patterns (Prenter 1975; Wahba 1990). Typically, a spline approximation that minimizes a regularized version of the objective function (B2) is sought. Inoue (1986) has used a standard regularization term

$$\mathcal{R}(u) \equiv \tilde{w}^{10}\left\|\frac{\partial}{\partial x}u\right\|^2 + \tilde{w}^{01}\left\|\frac{\partial}{\partial y}u\right\|^2 + \tilde{w}^{20}\left\|\frac{\partial^2}{\partial x^2}u\right\|^2 + \tilde{w}^{02}\left\|\frac{\partial^2}{\partial y^2}u\right\|^2 + \tilde{w}^{11}\left\|\frac{\partial^2}{\partial x \partial y}u\right\|^2 \quad \text{(B3)}$$

(the so-called thin plate model), where $\tilde{w}^{il}$ are the weights that constrains the roughness of the solution field. Given a particular sampling pattern of the data, methods to choose optimal values for these regularization weights can be considered (Bauer et al. 1997), although qualitative judgment of the interpolated field is still necessary in practice (Inoue 1986). The regularized approximation problem then becomes

$$\min_{u(x,y)} \int_{-\infty}^{\infty} \int_{-\infty}^{\infty} \mathcal{S}(u) + \mathcal{R}(u)\, dx\, dy. \quad \text{(B4)}$$

By substituting in the spline approximation (B1) for $u(x, y)$, this minimization problem becomes finitely vectorized, and the minimizing set of spline coefficients can be obtained as the solution of the sparse and linear system of equations

$$\sum_{m=1}^{M} \sum_{n=1}^{N} A_{pqmn}B_{mn} = E_{pq}, \qquad p = 1, 2, \ldots, M, \quad q = 1, 2, \ldots, N, \quad \text{(B5)}$$

defined by the parameters

$$A_{pqmn} = \tilde{w}^{10}\tilde{I}^{10}_{p-m,q-n} + \tilde{w}^{01}\tilde{I}^{01}_{p-m,q-n} + \tilde{w}^{20}\tilde{I}^{20}_{p-m,q-n} + \tilde{w}^{02}\tilde{I}^{02}_{p-m,q-n} + \tilde{w}^{11}\tilde{I}^{11}_{p-m,q-n} + \sum_{k=1}^{K} \tilde{w}_k^d\beta(\tilde{x}_k - p)\beta(\tilde{y}_k - q)\beta(\tilde{x}_k - m)\beta(\tilde{y}_k - n)$$

and

$$E_{pq} = \sum_{k=1}^{K} \tilde{w}_k^d\tilde{u}_k\beta(\tilde{x}_k - p)\beta(\tilde{y}_k - q),$$

where the precomputable definite integrals $\tilde{I}^{il}_{p-m,q-n}$ are given by

$$\tilde{I}^{il}_{p-m,q-n} \equiv \int_{-\infty}^{\infty} \int_{\infty}^{\infty} \frac{\partial^i}{\partial x^i}\beta(x)\frac{\partial^i}{\partial x^i}\beta(x + p - m)\frac{\partial^l}{\partial y^l}\beta(y)\frac{\partial^l}{\partial y^l} \times \beta(y + q - n)\, dx\, dy.$$

Because of the compact support of the cubic B-spline function, most A_{pqmn}'s are zero. In particular, the cubic B-spline (5) has a support of $x \in [-2, 2]$, and a matrix version of the corresponding (B5) is in fact a nested septidiagonal system. Inoue (1986) provides a FORTRAN code to set up this linear system of equations.

In summary, under this scheme, computation of the

spline coefficients B_{jmn} amounts to solving the sparse system of linear equations (B5) for each j, given the measured and precomputed quantities denoted by symbols with tildes (˜).

REFERENCES

Attema, E. P. W., 1991: The active microwave instrument on-board the *ERS-1* satellite. *Proc. IEEE,* **79,** 791–799.

Barnier, B., M. Bonkthir, and J. Verron, 1991: Use of satellite scatterometer wind data to force a general circulation ocean model. *J. Geophys. Res.,* **96** (C12), 22 025–22 042.

——, J. Capella, and J. J. O'Brien, 1994: The use of satellite scatterometer winds to drive a primitive equation model of the Indian Ocean: The impact of bandlike sampling. *J. Geophys. Res.,* **99** (C7), 14 187–14 196.

Battle, G., 1987: A block spin construction of ondelettes. Part I: Lemarié functions. *Comm. Math. Phys.,* **110,** 601–615.

Daubechies, I., 1992: *Ten Lectures on Wavelets.* Society for Industrial and Applied Mathematics, 357 pp.

Farge, M., 1992: Wavelet transforms and their applications to turbulence. *Annu. Rev. Fluid Mech.,* **24,** 395–457.

Freilich, M. H., and D. B. Chelton, 1986: Wavenumber spectra of Pacific winds measured by the Seasat scatterometer. *J. Phys. Oceanogr.,* **16,** 741–757.

——, and ——, 1993a: Derivation of satellite wind model functions using operational surface wind analyses: An altimeter example. *J. Geophys. Res.,* **98** (C8), 14 633–14 649.

——, and ——, 1993b: A preliminary C-band scatterometer model function for the *ERS-1* AMI instrument. *Proc. First ERS-1 Sympo.,* Cannes, France, ESA, 79–84.

——, and J. D. Pazdalski, 1995: Wavenumber spectra of surface wind kinetic energy and wind stress curl from *ERS-1* scatterometer data. *1995 ADEOS/NSCAT Science Working Team Meeting,* Kyoto, Japan, ADEOS/NSCAT, 165–172.

Heijmans, H. J. A. M., 1993: Discrete wavelets and multiresolution analysis. *Wavelets: An Elementary Treatment of Theory and Applications.* T. H. Koorwinder, Ed., World Scientific Publishing, 49–79.

Hellerman, S., and M. Rosenstein, 1983: Normal monthly wind stress over the world ocean with error estimates. *J. Phys. Oceanogr.,* **13,** 1093–1104.

Inoue, H., 1986: A least-squares smooth fitting for irregularly spaced data: Finite-element approach using the cubic B-spline basis. *Geophysics,* **51,** 2051–2066.

Large, W. G., and S. Pond, 1981: Open-ocean momentum flux measurements in moderate to strong winds. *J. Phys. Oceanogr.,* **11,** 324–336.

——, W. R. Holland, and J. C. Evans, 1991: Quasigeostrophic ocean response to real wind forcing: The effects of temporal smoothing. *J. Phys. Oceanogr.,* **21,** 998–1017.

Leith, C. E., 1971: Atmospheric predictability and two-dimensional turbulence. *J. Atmos. Sci.,* **28,** 145–161.

Lemarié, P. G., 1988: Ondelettes à localisation exponentielles. *J. Math. Pures Appl.,* **67,** 227–236.

Mallat, S. G., 1989: A theory for multiresolution signal decomposition: The wavelet representation. *IEEE Trans. Pattern Analysis Machine Intelligence,* **11,** 674–693.

Mariano, A. J., and O. Brown, 1992: Efficient objective analysis of dynamically heterogeneous and nonstationary fields via the parameter matrix. *Deep-Sea Res.,* **39,** 1255–1271.

Meneveau, C., 1991: Analysis of turbulence in the orthonormal wavelet representation. *J. Fluid Mech.,* **232,** 469–520.

Milliff, R. F., W. G. Large, W. R. Holland, and J. C. McWilliams, 1996: The general-circulation responses of a high-resolution North Atlantic ocean models to synthetic-scatterometer winds. *J. Phys. Oceanogr.,* **26,** 1747–1768.

Naderi, F. M., M. H. Freilich, and D. G. Long, 1991: Spaceborne radar measurement of wind velocity over the ocean—An overview of the NSCAT scatterometer system. *Proc. IEEE,* **79,** 850–866.

Perrier, V., T. Philipovitch, and C. Basdevant, 1995: Wavelet spectra compared to Fourier spectra. *J. Math. Phys.,* **36,** 1506–1519.

Prenter, P. M., 1975: *Splines and Variational Methods.* Wiley, 323 pp.

Unser, M., and A. Aldroubi, 1992: Polynomial splines and wavelets—A signal processing perspective. *Wavelets—A Tutorial in Theory and Applications.* C. K. Chui, Ed., Academic Press. 91–122.

Wahba, G., 1990: *Spline Models for Observational Data.* Society for Industrial and Applied Mathematics, 169 pp.

Wornell, G. W., 1993: Wavelet-based representations for the $1/f$ family of fractal processes. *Proc. IEEE,* **81,** 1428–1450.

Yamada, M., and K. Ohkitani, 1991: An identification of energy cascade in turbulence by orthonormal wavelet analysis. *Progr. Theor. Phys.,* **86,** 799–815.